Failure investigation of a geosynthetic-reinforced soil slope subjected to rainfall

K.-H. Yang[1], J. N. Thuo[2], J.-W. Chen[3] and C.-N. Liu[4]

[1]*Associate Professor, Department of Civil Engineering, National Taiwan University (NTU), 1, Sec. 4, Roosevelt Rd., Taipei 106, Taiwan, E-mail: khyang@ntu.edu.tw (corresponding author)*
[2]*Lecturer, Department of Civil Engineering, Dedan Kimathi University of Technology, Kenya, E-mail: joseph.thuo@dkut.ac.ke*
[3]*Research and Development Substitute Services, Research and Technology Development Team, Soil and Water Conservation Bureau, Taiwan, E-mail: wiwi820217@gmail.com*
[4]*Professor, Department of Civil Engineering, National Chi-Nan University, Taiwan, E-mail: cnliu2009@gmail.com*

Received 26 February 2018, revised 01 August 2018, accepted 07 August 2018, published 12 October 2018

ABSTRACT: This paper presents a comprehensive failure investigation of a geosynthetic-reinforced soil (GRS) slope subjected to rainfall. The investigated slope is a 26-m high, four-tier, geogrid-reinforced structure backfilled with low plasticity silty clay that contains more than 60% of fines. The GRS slope first exhibited excessive deformation after typhoons and heavy rainfall from 2010 to 2012. The slope collapsed in 2013 due to two sequential typhoon events with a total accumulated rainfall of more than 600 mm. The slope failed in a compound failure mode in which the failure surface partially cut through the reinforced zone and partially passed along the interface between the weathered sandstone and intact shale. By using the recorded rainfall, site geology, and measured soil and reinforcement parameters, a series of coupled hydro-mechanical finite element analyses were performed on the basis of the unsaturated soil mechanics to examine the failure mechanism and factors triggering the slope failure. The numerical results indicated that the slope failure occurred due to the development of positive porewater pressure within the reinforced zone and retained weather sandstone layer. Observations and lessons learned from this case history are discussed and remedial measures to improve the overall slope stability are proposed and evaluated.

KEYWORDS: Geosynthetics, Reinforced slope, Marginal backfill, Rainfall infiltration, Failure, Coupled hydro-mechanical analysis

REFERENCE: Yang, K.-H., Thuo, J. N., Chen, J.-W. and Liu, C.-N. (2019). Failure investigation of a geosynthetic-reinforced soil slope subjected to rainfall. *Geosynthetics International*, **26**, No. 1, 42–65. [https://doi.org/10.1680/jgein.18.00035]

1. INTRODUCTION

Geosynthetic-reinforced soil (GRS) structures are widely constructed because of their economic advantages and successful performance. GRS structures are typically composed of four components: backfill soil, reinforcement, facing, and drainage. Among these components, the backfill material has a major effect on the suitability and applicability of the GRS structures – for example, cost, transportation, environmental concern, and stability (Christopher and Stuglis 2005; Raisinghani and Viswanadham 2011). Design guidelines (Elias *et al*. 2001; AASHTO 2002; Berg *et al*. 2009; NCMA 2010) suggest the use of good quality soil (i.e. granular soil) as backfill, because of its high permeability, for preventing the development of porewater pressure (PWP) within the soil. Figure 1 displays the gradation limits for backfills suggested in the design guidelines. In addition to the gradation limits, the plasticity index of the backfill is also specified (PI $\leq$ 6 and 20 for walls and slopes, respectively). Notwithstanding that the use of fine-grained soils as backfill does not meet the grain size recommendations specified in the design guidelines (usually referred to as marginal fills), many areas where granular backfill is not readily available adopted locally available soils containing certain fines as alternative backfills to minimize transportation cost and environmental impact. Moreover, the marginal soils were adopted to adhere to a local regulation that specifies that the excavated and backfilled soils at the construction site should be balanced.

The low draining capacity of fine soils has been reported to compromise performance of reinforced soil walls upon wetting by rainfall infiltration or groundwater seepage due to the build-up of PWP within backfills

Downloaded by [International Geosynthetics Society] on [26/03/20]. Copyright © ICE Publishing, all rights reserved.

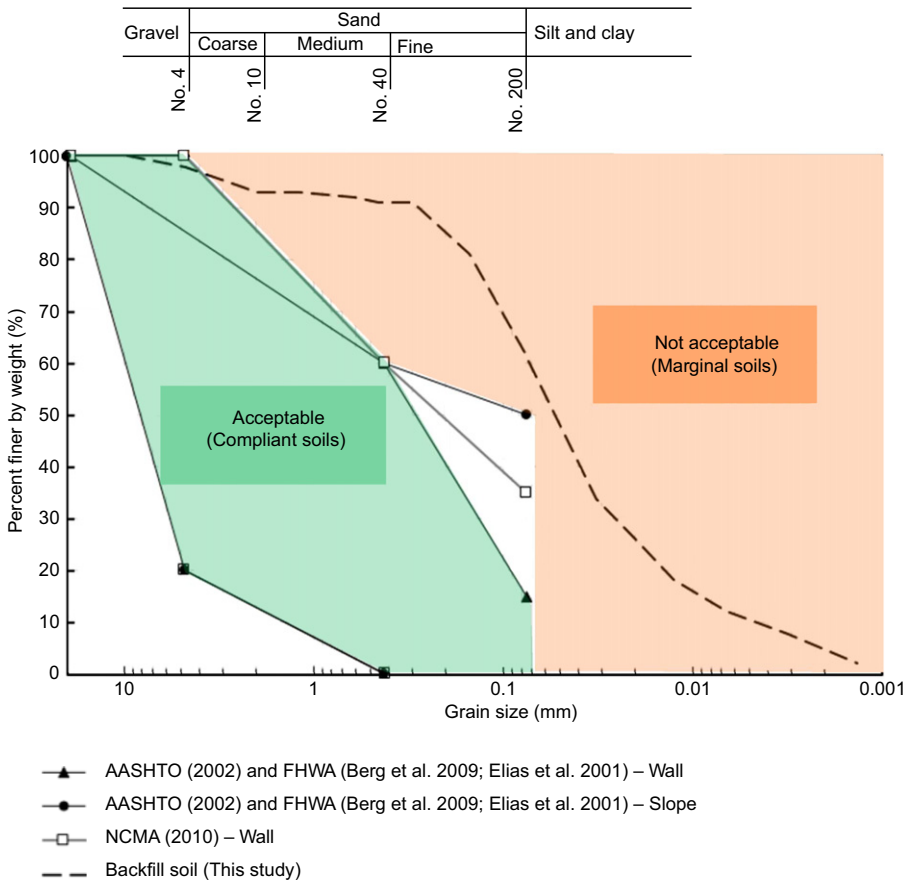

Figure 1. Grain size distribution of backfill in this study and as recommended by design guidelines

(Zornberg and Mitchell 1994; Mitchell and Zornberg 1995; Yoo and Jung 2006; Koerner and Koerner 2013; Valentine 2013). Koerner and Koerner (2013) investigated 171 failure cases of GRS structures that experienced excessive deformation or collapse. The statistical data from the investigated GRS structures revealed that 61% of the failed cases had used silt or clay as backfill and 60% were caused by internal or external water. The practical significance, design guidance, and drainage considerations for GRS structures with marginal backfills have been discussed by Christopher and Stuglis (2005), Christopher *et al.* (1998), and Raja *et al.* (2012). These studies have advocated that implementation of proper quality control and inspection programs during construction and installation of adequate drainage systems to alleviate PWP accumulation within backfills are the two major tasks that should be conducted to ensure the stability of GRS structures with marginal backfills.

Many experimental and numerical studies have been performed to understand the behavior and performance of GRS structures with marginal backfills, especially under rainfall or seepage conditions (Iryo and Rowe 2005; Garcia *et al.* 2007; Raisinghani and Viswanadham 2011; Portelinha *et al.* 2013; Portelinha and Zornberg 2014, 2017; Bhattacherjee and Viswanadham 2015; Hatami and Esmaili 2015; Thuo *et al.* 2015; Balakrishnan and Viswanadham 2016; Vahedifard *et al.* 2016b, 2017; Bui Van *et al.* 2017; Chinkulkijniwat *et al.* 2017; Viswanadham *et al.* 2017; Yang *et al.* 2018). Excellent reviews of case histories, applications, and soil-reinforcement interaction of reinforced soil structures with poorly draining backfill have been provided by Mitchell and Zornberg (1995) and Zornberg and Mitchell (1994).

In contrast to the aforementioned studies, only a few references in literature have reported case studies of GRS structures that failed due to seepage and rainfall infiltration. Shibuya *et al.* (2007) reported a 23 m reinforced wall failure in Japan due to typhoon-induced heavy rainfall. The reinforced wall was backfilled with locally weathered silty soil which had a fines content of over 25%. The factors that caused wall failure were the concentration of in-soil seepage and surface water flow into the backfill, the use of low-permeability soil as backfill, a poor drainage system behind the wall, and the low bearing capacity of the foundation. Yoo and Jung (2006) investigated a 7.4 m reinforced wall failure in Korea caused by heavy rainfall during a monsoon. The backfill consisted of completely decomposed granite soil available at the site; approximately 25% of the backfill consisted of fines. The causes that contributed to the wall failure were an inadequate design due to improper modeling of the wall system, including the topology, an ignorant analysis of the global slope stability, the use of low-quality soil as backfill, overestimation of the internal friction angle of the soil, and the construction defect of not waterproofing the top surface of the reinforced zone. Liu *et al.* (2012) studied a 40 m high steep geogrid-reinforced slope in Taiwan that

Downloaded by [International Geosynthetics Society] on [26/03/20]. Copyright © ICE Publishing, all rights reserved.

failed three times in 1994, 1999, and 2004 due to rainfall infiltration after a long rainy season, the Chi-Chi earthquake, and typhoon-induced torrential rainfall, respectively. The soil in the backfill zone was weathered laterite soil containing approximately 42% of fines. The factors that caused the wall failures were poor site investigation that could not identify a weak, impermeable clay layer behind the backfill zone; lack of a sub-drainage system; and ignorance in analyzing the global slope stability. Kim and Borden (2013) conducted a numerical study to evaluate a 5.4 m GRS wall built in North Carolina, USA, which experienced an excessive deformation and localized collapse during a rainy season that continued for a few months after completing the wall construction. Low-plasticity clayey soil with approximately 60% of fines was used as the backfill. In addition to using marginal soils as backfills, the poor compaction quality of soils is another major problem that can cause unsatisfactory performance for GRS walls. The low as-compacted water content and low-quality compaction zone in the vicinity of the wall face caused the soil shear strength and stiffness to significantly reduce as surface water infiltration occurred.

This study conducts a comprehensive failure investigation of a GRS slope with marginal backfill in Taichung, Taiwan. The GRS slope first experienced excessive deformation after typhoons and heavy rainfall from 2010 to 2012. The slope finally collapsed in August 2013 due to two sequential typhoon events with a total accumulated rainfall of more than 600 mm. A series of coupled hydro-mechanical finite element (FE) analyses on the basis of the unsaturated soil mechanics framework were conducted. Field and laboratory test data obtained from site investigations were applied as input material properties and initial conditions to the numerical model. The objectives of this paper involve (1) investigation of the failure mechanisms and factors triggering the specific GRS slope failure in Taichung, Taiwan; (2) establishment and validation of a numerical model for predicting GRS slope failure considering transient seepage and soil unsaturated conditions; (3) assessment of potential remedial measures to mitigate catastrophic damage and failure of GRS structures due to heavy rainfall; and (4) suggestion of the design and construction implications for GRS structures with marginal backfill.

First, this paper introduces the case history of the investigated GRS slopes. The design, construction, site conditions, hydrological information, and the factors causing the slope failure are discussed. Second, limitations of conventional design methods based on limit equilibrium methods for analyzing the slope stability of GRS structures during rainfall are highlighted. Third, the coupled hydro-mechanical FE analysis theory is introduced. Fourth, coupled hydro-mechanical FE analyses are performed to examine the failure mechanism, PWP distribution, and mobilization of reinforcement tensile loads of the GRS slope. Fifth, on the basis of the revealed failure mechanism, the potential remediation measures to improve the overall slope stability are proposed and evaluated. The lessons learned from the findings of this study are discussed at the end of this paper. The results and discussion of this study provide insightful information and a unique opportunity to examine the behavior and design of, and mitigation measures for GRS structures with marginal backfill against rainfall infiltration.

2. CASE HISTORY OF THE GRS SLOPE

2.1. Slope and site conditions

The investigated GRS slope was located in a mountainous area of Taichung, Taiwan. The GRS slope was constructed to stabilize a natural slope consisting of weathered sandstone that provides traffic access to a landfill site. Figure 2 displays the cross-section of the GRS slope and geological conditions at the site where the slope failure occurred.

The geological formation of the site comprised a highly weathered and fractured sandstone layer (WR) underlain by a fresh intact shale, interbedded with a small amount of sandstone (SH/ss) (Figure 2). An access road to the landfill management center and the landfill site at the top of the hill was just beside the toe of the bottom tier and the crest of the topmost tier of the GRS slope. A creek runs a few meters below the slope, thus indicating that the groundwater table level, under normal conditions, is near the slope's toe. The annual average precipitation in the Taichung area is 1642 mm/year, mostly concentrated during the plum rain (the East Asian rainy season) and the typhoon season, from May to October (Shou *et al.* 2018).

The 20–27 m high and 60 m long GRS slope has an inclination angle of $0.5H$: $1V$ ($= 63°$). The GRS slope comprises four tiers, each with a height and offset distance between two adjacent tiers in the ranges of 4–8 m and 2–4 m, respectively (Figure 2). The reinforcement is PET geogrid with an opening size of 15 mm × 25 mm and opening ratio of 45%. The geogrid layout in each tier had a length in the range of 6–8 m and vertical spacing of 0.5 m, and was wrapped around sandbags at both its front and rear ends. Locally available soil from the weathered shale and sandstone was used as the backfill in the reinforced zone. Figure 1 displays the grain size distribution curve of the backfill soil. The use of the marginal soils as backfill might have been motivated by a desire to minimize the cost and environmental impact associated with the transportation of recommended backfills to the construction site and the disposal of excavated in-situ soils. In contrast to the backfill recommendations in the design guidelines, the backfill soil contained more than 60% of fines. The soil was classified as CL-ML (low plasticity silty clay) according to the Unified Soil Classification System (USCS) (ASTM D2487) with a specific gravity $G_s = 2.66$, plastic limit PL = 16.6%, liquid limit LL = 20.9%, and plasticity index PI = 4.3%. In Figure 1, the entire grain size distribution curve of the backfill is within the marginal soil zone suggested by the design guidelines (Elias *et al.* 2001; AASHTO 2002; Berg *et al.* 2009; NCMA 2010). Detailed engineering properties of soil and reinforcement are discussed in Section 4.2.

For field compaction, soils were compacted using drum rollers on every 30 cm lift of soil and required to reach to a

Downloaded by [International Geosynthetics Society] on [26/03/20]. Copyright © ICE Publishing, all rights reserved.

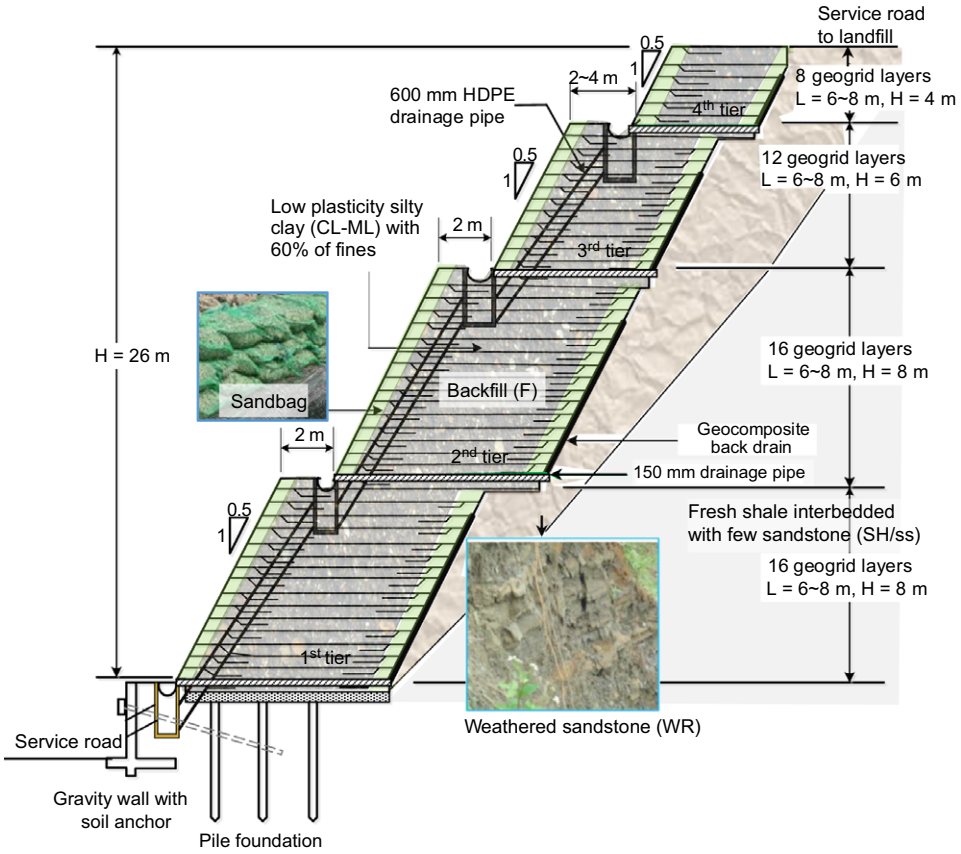

Figure 2. Layout and design details of multi-tier GRS slope

relative compaction $R_c = 90\%$ with respect to the modified proctor compaction test results. However, during construction, the contractor had been warned that the inspection frequency for the field density was considerably less than the required inspection frequency. Besides, it was also found that the compaction had not been executed rigorously at each soil lift. The GRS slope was supported by a piled foundation consisting of a group of drilled shafts. In addition, an existing retaining structure system (a gravity wall with soil anchors) was situated right in front of the piled foundation.

For drainage (Figures 2 and 3), geocomposite back drains were placed at a spacing of 2 m at the interface between the backfill and the natural slope. Transverse 150 mm diameter drainage pipes, spaced at 2 m, were laid adjacent to the geocomposite back drains at the bottom of each tier to transfer water from the back to the front of the slope. The transverse pipes were perforated to allow the pore water from the backfill to seep into the pipe. The transverse drains were wrapped in nonwoven geotextile to prevent soil particles from clogging the surficial holes or intruding into the pipe. The 600 mm vertical drainage pipes were installed near the front facing of the slope to drain the surficial runoff collected by the open drainage ditches at the toe of each tier. The concerns of the original drainage design are:

- The drainage joints either between the back drain and transverse pipe (Figure 3a) or between the drainage ditch and vertical pipe (Figure 3b) were poorly and loosely connected. No flexible joint was applied at the connection. When the slope deformed, these joints could easily become disconnected, and consequently the drainage system could malfunction.
- The nonwoven geotextile served as a filter layer between the drainage pipes and backfill soil (Figure 3c); however, the filtration function of the geotextile had not been evaluated according to geotextile filtration criteria such as soil retention, clogging resistance, and the permeability of the geotextile. Because the backfill contains a high percentage of fines, it is suspected that the nonwoven geotextile could be clogged by fine soil particles, thus leading to a reduction in the system drainage capacity in the long term.
- No drainage ditch was designed for the top of the slope (i.e. the top of the fourth tier) to collect the surficial runoff and guide the water out of the slope. When the slope deformed, the surficial water could easily pond and then infiltrate into the slope.

2.2. Slope history and failure

The GRS slope construction began on January 2010 and was completed on September 2010. Figure 4 displays a summary of the slope history and satellite images at different times from Google Earth. During its service life, the slope was exposed to several rainy seasons consisting of the plum rain and typhoon from May to October. On July 2010, 2 months prior to the completion of construction, a landfill worker discovered tension cracks and slope

Downloaded by [International Geosynthetics Society] on [26/03/20]. Copyright © ICE Publishing, all rights reserved.

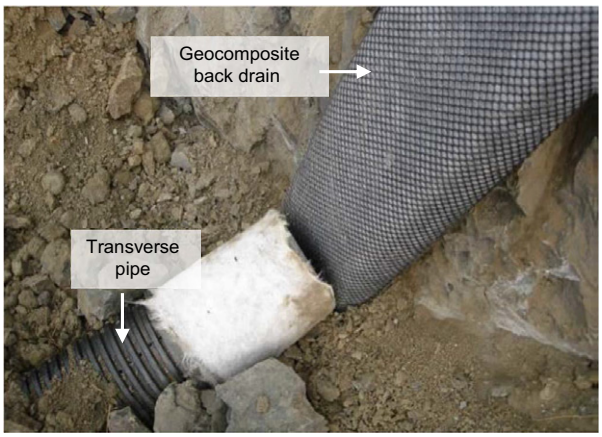

(a)

(b)

(c)

Figure 3. Drainage system: (a) joint between back drain and transverse pipe; (b) joint between drainage ditch and vertical pipe; (c) transverse pipe wrapped in nonwoven geotextile (images provided by Taiwan Professional Geotechnical Engineers Association)

settlement at the top of the slope. The tension cracks and slope settlement were caused by a series of heavy rainfall events brought by the moist south-westerly winds from June to July 2010. The slope settlement was repaired during the period from January to April 2011 by placing additional backfill on the top of the slope to compensate for the settlement that had already occurred. No noticeable tension crack or slope settlement was observed in 2011 after the slope had been backfilled because no significant amount of rainfall occurred in that area during the rainy season of 2011.

During the rainy season of 2012, the slope was subjected to a significant amount of rainfall from the plum rain (total precipitation $R = 187$ mm) in May, Typhoon Talim ($R = 350$ mm) in June, torrential rainfall ($R = 243$ mm) in July, and Typhoon Saola ($R = 563$ mm) in August. During this period, tension cracks and slope settlement regenerated and gradually developed as the rainfall continued. Figure 5 displays subsequent photographs of the development of the tension cracks and slope settlement with time. A slope monitoring program was immediately initiated to measure the top settlement and facing deflection of the third and fourth tiers of the GRS slope for a period of 7 months from June to December 2012. On the basis of the monitoring results, the maximum slope settlement and facing deflection measured on the fourth tier approached 140 and 80 cm, respectively. Figure 6 illustrates the measured slope settlement at different locations (A01–03, as shown in the insert in Figure 6) on the top of the fourth tier during this period. Clearly, the slope settlement directly correlated to rainfall: the slope settlement substantially developed from June to September 2012 during the rainy season and stopped intensifying from October to December 2012, when slight rainfall was observed. The slope was repaired again, and the top of the slope was waterproofed with a layer of controlled low strength material (CLSM) underlain by a geomembrane to prevent rainfall infiltration.

The slope finally collapsed on 1 September 2013, which is around 3 years after completing the construction of the slope. The slope collapse was triggered by two consecutive typhoon events – Typhoon Trami ($R = 338$ mm) from 20 to 24 August 2013, and Typhoon Kongrey ($R = 310$ mm) from 29 August to 1 September 2013. Although the total precipitation of Typhoon Kongrey was less than that of Typhoon Saola in 2012, the two typhoon events occurred almost continuously and brought a total precipitation of 648 mm within 10 days. This comparison suggests the antecedent rainfall (i.e. the rainfall event prior to the major rainfall event) has an important role in influencing the stability of the GRS slope.

Figure 7 displays photographs of the slope failure. The total width of failure area was approximately in the range of 30–50 m (Figure 7a). Figure 8 depicts the location of the observed failure surface. The slope failed in a compound failure mode: the failure surface partially cut through the reinforced zone at approximately one-third height of the first tier and partially passed along the interface between the weathered sandstone and intact shale. The bottom of the GRS slope moved out translationally and was suspended from the existing retaining wall (Figure 7b). A visual inspection conducted after the rain ceased demonstrated that water continued to seep out from the failure part of the backfill (Figure 7b). This finding suggested that the soil had a high moisture condition, likely full saturation, and positive PWP

Downloaded by [International Geosynthetics Society] on [26/03/20]. Copyright © ICE Publishing, all rights reserved.

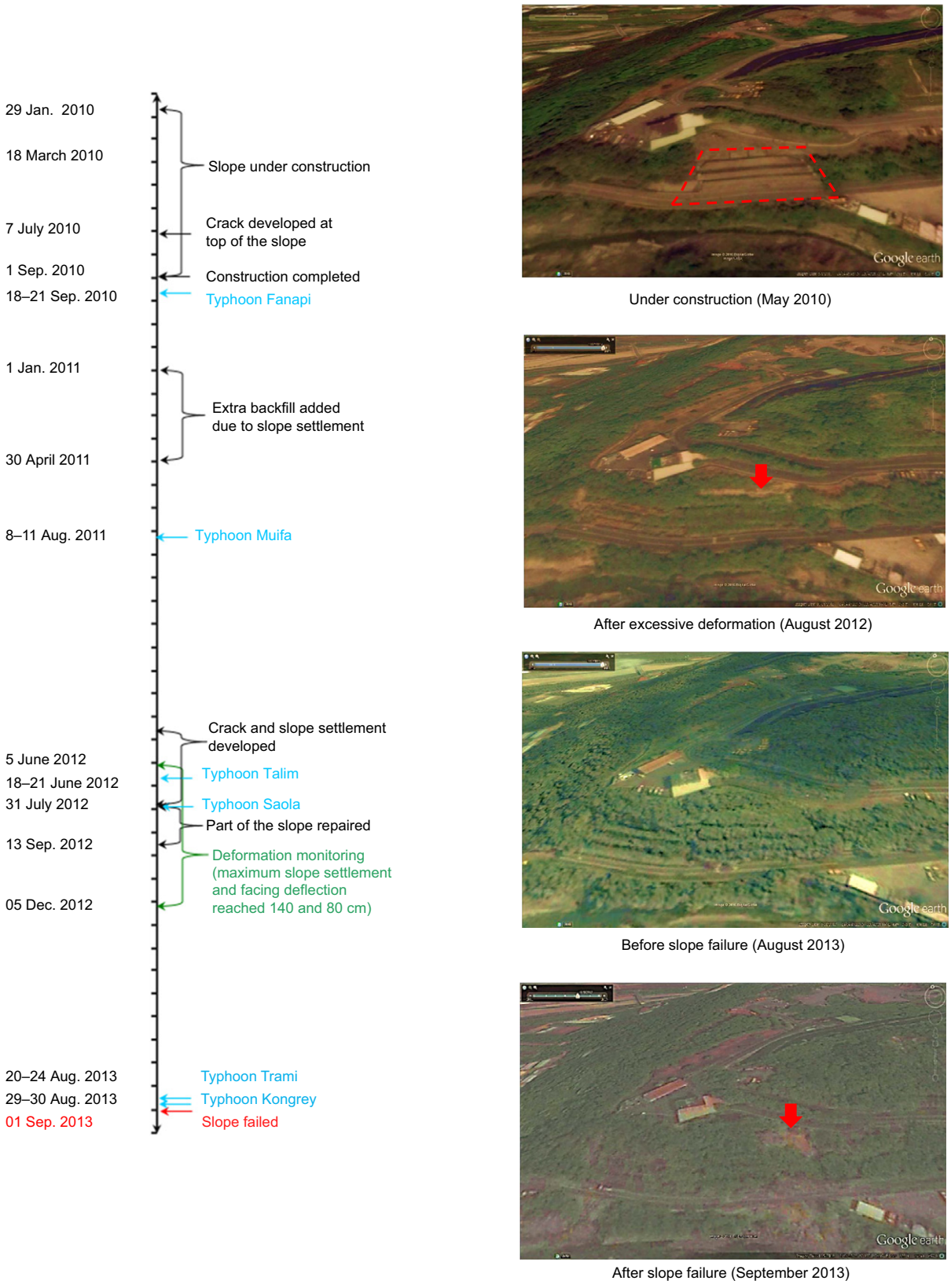

Figure 4. Summary of slope history and satellite photographs from Google earth

possibly accumulated within the backfill after several days of rain. Moreover, water was found to pond on the road pavement retained by the debris of the backfill soil, thus indicating that the soil possesses low permeability (Figure 7c).

The factors that caused the slope failure concluded from the forensic investigation are summarized as follows:

- The use of marginal soil (over 60% of fines) as the backfill was contrary to the backfill

Downloaded by [International Geosynthetics Society] on [26/03/20]. Copyright © ICE Publishing, all rights reserved.

(a)

(b)

(c)

Figure 5. Development of tension crack and slope settlement during the rainy season in 2012: (a) tension crack; (b) onset of settlement; (c) excessive settlement over 1 m (images provided by Taiwan Professional Geotechnical Engineers Association)

recommendations in the design guidelines. High soil moisture content and PWP developed within the marginal backfill when the slope was subjected to rainfall infiltration.

- The original design and site investigation overlooked the existence of the weathered and fractured rock layer, which has shear strength less than that of an intact rock.
- The tension cracks and slope settlement developed at the top surface of the slope allows rain water to pond up on the slope top and consequently to infiltrate into the reinforced zone.
- The drainage system may have malfunctioned because drainage joints were poorly and loosely connected during the construction and likely dislocated due to the excessive slope deformation.
- The use of a nonwoven geotextile as a filter layer was not evaluated by the geotextile filtration criteria. The nonwoven geotextile filter could be clogged by fine soil particles and thus could impair or disable the system drainage capacity.
- No drainage ditch was designed for the top of the slope to collect the surficial runoff and guide the water out of the slope.

2.3. Design method and limitations

In the original design, the slope stability analyses were performed using the modified Bishop method as coded in the STEDwin software. The calculated factor of safety (FS) of the GRS slope under normal, heavy rainfall, and earthquake conditions were FS = 1.60, 1.30, and 1.43, respectively. For the analysis under the heavy rainfall condition, the effects of rainfall on a slope are typically modeled by raising the phreatic level in a slope. In the original design, the phreatic surface was assumed at the interface between the backfill and natural slope for the analysis under the heavy rainfall condition. However, as later shown in the result of the coupled hydro-mechanical analysis, the predicted phreatic surface location differs from the one assumed in the original slope stability analysis. The limitations of conventional methods to analyze the stability of a slope subjected to rainfall are discussed as follows:

- The location of the phreatic surface under rainfall conditions must be assumed. This approach is especially challenging for the fill-type retaining structure because no groundwater monitoring data is available before the retaining structure is built. An assumption of an incorrect phreatic level could cause inaccurate prediction of the corresponding FS.
- The approach of raising the phreatic level only considers the change in the effective stress of saturated soil below the phreatic surface, which may overlook the influence of rainfall infiltration on unsaturated soil within the wetting front. The variation of PWP and soil shear strength within retaining structures as soil changes from unsaturated to saturated conditions cannot be modeled appropriately, which can result in a misinterpretation of the failure mechanism and an inaccurate prediction of the FS.
- The impact of the rainfall intensity and effect of the soil hydraulic conductivity and drainage system cannot be effectively evaluated. Engineers can only design drainage systems empirically without the flexibility of adjusting the drainage system on the basis of different soil types and rainfall intensities.

The second problem in the original design is that the external stability of the slope was not evaluated. On the basis of the field observation and numerical interpretation as discussed later, the GRS slope was pushed by the lateral earth pressure, and sliding occurred at the bottom of the slope as the phreatic surface within the slope rose to a critical level. To evaluate the external stability of the GRS slope against sliding, the conventional sliding

Downloaded by [International Geosynthetics Society] on [26/03/20]. Copyright © ICE Publishing, all rights reserved.

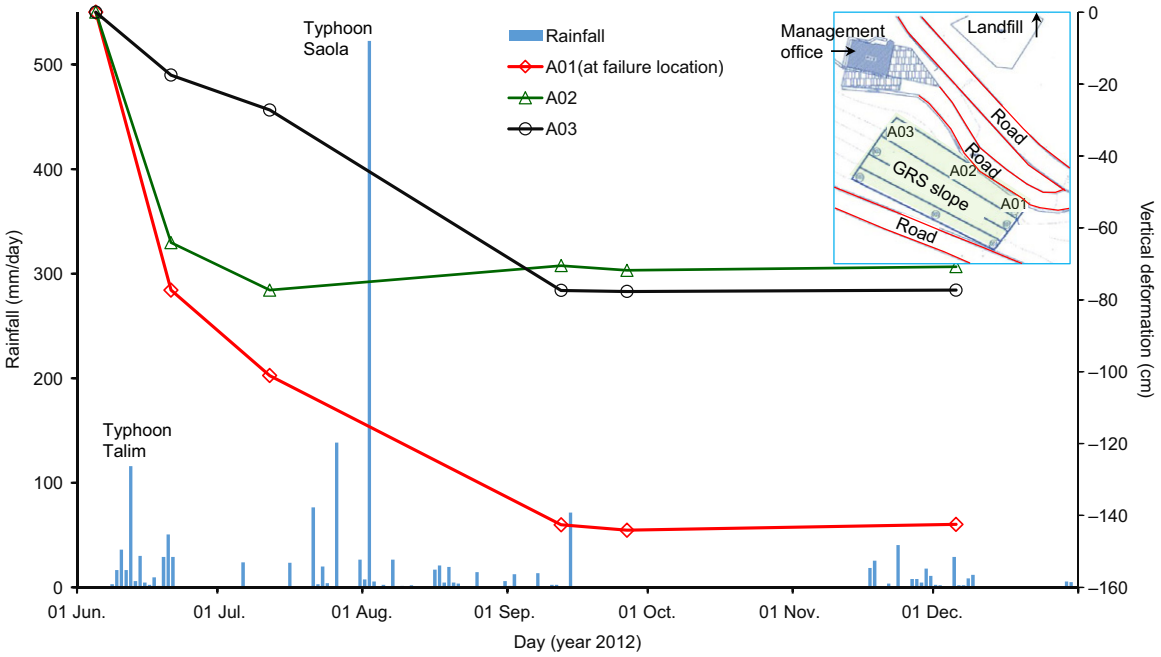

Figure 6. Relationships between rainfall and slope settlement (negative deformation value indicates settlement)

block analysis (Samtani and Nowatzki 2006; Elias *et al.* 2001; Berg *et al.* 2009) was performed by assuming that the GRS slope was a rigid block subjected to the driving forces consisting of active earth pressure from the weathered sandstone and PWP accumulated at the slope back. The effect of suction could affect the earth pressure (Vahedifard *et al.* 2015, 2016a 2016b), but it was not included in the analysis of external stability because this effect is typically not considered in the conventional design. Figure 9 displays the calculated FS against sliding under various assumed phreatic levels. Clearly, the sliding failure occurred (FS < 1) when the phreatic surface rose near the top of the first tier. This phreatic level is in agreement with the level predicted by the coupled hydro-mechanical analysis presented later.

3. FORMULATIONS OF COUPLED HYDRO-MECHANICAL ANALYSIS

Because the conventional method has limitations in analyzing the stability of a slope subject to rainfall, the coupled hydro-mechanical analysis based on the framework of unsaturated soil mechanics was conducted in this study to appropriately describe the hydraulic and mechanical responses of soil when soil transfers from the unsaturated to saturated conditions. Therefore, more accurate and realistic assessment of the slope stability and failure mechanism is obtained under rainfall conditions. The theory and formulations of the coupled hydro-mechanical analysis are introduced in this section.

3.1. Governing equation

The fully coupled flow deformation module was implemented into the PLAXIS (version 2D 2015) FE program to consider the deformation and seepage flow within the partially saturated soil. Galavi (2016) reported detailed FE formulations and verification for the coupled hydro-mechanical analysis. The coupled hydro-mechanical formulation was developed on the basis of Biot's three-dimensional consolidation theory, which involves two sets of governing equations—partial differential force equilibrium and continuity equations:

$$\nabla^T(\underline{\boldsymbol{\sigma}}' + p\underline{\boldsymbol{m}}) + \underline{\boldsymbol{b}} = 0 \tag{1a}$$

$$-\nabla^T\left[\frac{\underline{\underline{\mathbf{k}}}}{\gamma_w}\left(\nabla p + \rho_w \underline{\boldsymbol{g}}\right)\right] = \frac{\partial}{\partial t}(n_p S) \tag{1b}$$

where ∇ is the first order differential operator; $\underline{\boldsymbol{\sigma}}'$ is the effective stress tensor; p is the pore pressure; $\underline{\boldsymbol{m}}$ is a vector with unity for normal stress and zero for shear stress; $\underline{\boldsymbol{b}}$ is the body force vector; $\mathbf{k}$ is the hydraulic conductivity matrix; γ_w and ρ_w are the unit weight and density of water, respectively; $\underline{\boldsymbol{g}}$ is the vector of gravitational acceleration; t is the time; n_p and S are the porosity and degree of saturation of soil, respectively; for a plane condition, $\underline{\boldsymbol{m}}^T = [1\ 1\ 1\ 0]$.

The governing equations form a coupling matrix from which the displacement and PWP can be solved simultaneously.

$$\begin{bmatrix} \underline{\underline{\mathbf{K}}} & \underline{\underline{\mathbf{Q}}} \\ 0 & -\underline{\underline{\mathbf{H}}} \end{bmatrix} \begin{bmatrix} \underline{\boldsymbol{u}} \\ \underline{\boldsymbol{p}} \end{bmatrix} + \begin{bmatrix} 0 & 0 \\ \underline{\underline{\mathbf{C}}} & -\underline{\underline{\mathbf{S}}} \end{bmatrix} \begin{bmatrix} \dot{\underline{\boldsymbol{u}}} \\ \dot{\underline{\boldsymbol{p}}} \end{bmatrix} = \begin{bmatrix} \underline{\boldsymbol{f}}_u \\ \underline{\boldsymbol{G}} + \underline{\boldsymbol{q}}_p \end{bmatrix} \tag{2}$$

where $\underline{\underline{\mathbf{K}}}$, $\underline{\underline{\mathbf{H}}}$, and $\underline{\underline{\mathbf{S}}}$ are the stiffness, permeability, and compressibility matrices, which are dependent on the state of stress and suction, respectively; $\underline{\underline{\mathbf{Q}}}$ and $\underline{\underline{\mathbf{C}}}$ are the coupling matrices; $\underline{\boldsymbol{u}}$ and $\underline{\boldsymbol{p}}$ are the vectors of incremental displacement and pore pressure, respectively; $\dot{\underline{\boldsymbol{u}}}$ and $\dot{\underline{\boldsymbol{p}}}$ are the vectors of displacement and pore pressure rate with respect to time, respectively; $\underline{\boldsymbol{f}}_u$, $\underline{\boldsymbol{q}}_p$, and $\underline{\boldsymbol{G}}$ are the vectors of

Downloaded by [International Geosynthetics Society] on [26/03/20]. Copyright © ICE Publishing, all rights reserved.

(a)

(b)

(c)

Figure 7. Slope failure: (a) Overview; (b) slope toe with water seeping out from backfill; (c) another view at the slope toe with water ponding (images provided by Taiwan Professional Geotechnical Engineers Association)

external load increment, input flux on boundaries, and the vertical flow driven by gravity, respectively.

Given that the third phase (pore air) within the surficial layer of the slope is essentially connected to the atmosphere, the air pressure in the unsaturated soil elements is assumed to have a constant value, thus causing the increment of air pressure to be equal to zero. This assumption enables the removal of the effect of air pressure from the coupled analysis. This approach has been adopted by many researchers in their studies of unsaturated slopes subjected to rainfall and seepage (Zhang *et al.* 2014; Oh and Lu 2015; Qi and Vanapalli 2015). Three-phase (soil, water, and air) coupled analysis should be considered for unsaturated earth structures that are subjected to seismic loadings, in which the unsaturated soils could be liquefied during earthquakes (Matsumaru and Uzuoka 2016).

3.2. Transient seepage analysis and soil–water characteristics

Before performing the coupled hydro-mechanical analyses, a transient seepage analysis was conducted to generate an initial PWP distribution. Soil deformation was not considered during the modeling of initial hydrological conditions. The applied governing equation of transient flow within an unsaturated medium was derived from Richards (1931):

$$k_x \frac{\partial^2 h}{\partial x^2} + k_y \frac{\partial^2 h}{\partial y^2} = \frac{\partial \theta}{\partial t} = m_w \rho_w \boldsymbol{g} \frac{\partial h}{\partial t} \tag{3}$$

where k_x and k_y represent the hydraulic conductivities in the x and y directions, respectively, (the k value is a function of matric suction); h is the total hydraulic head of flow; θ is the volumetric water content; m_w is the coefficient of water volume change (slope of the water characteristic curve); ρ_w is the density of water; $\boldsymbol{g}$ is the acceleration of gravity, and t is time.

In this study, the van Genuchten–Mualem model (Mualem 1976; van Genuchten 1980) was applied to define the relationship between matric suction and soil volumetric water content and to estimate changes in hydraulic conductivity with matric suction. The soil–water characteristics and k-function curves are expressed as follows:

$$\Theta = \frac{\theta - \theta_r}{\theta_s - \theta_r} = \left[\frac{1}{1 + \{\alpha(u_a - u_w)\}^n}\right]^{1-1/n} \tag{4}$$

$$k_{rel} = \frac{k}{k_s} = \Theta^{1/2}\left[1 - (1 - \Theta^{1/(1-1/n)})^{1-1/n}\right]^2 \tag{5}$$

where Θ is the normalized volumetric water content; θ_s is the saturated volumetric water content; θ_r is the residual volumetric water content; $u_a - u_w$ is the matric suction (where u_a and u_w are the pore air and pore water pressures, respectively); α and n are the curve fitting parameters in the van Genuchten–Mualem model; k_{rel} is the relative hydraulic conductivity; k is the hydraulic conductivity at any degree of soil saturation; and k_s is the saturated hydraulic conductivity.

3.3. Effective stress and shear strength under unsaturated conditions

The generalized effective stress principle was adopted in this study; that principle allows the soil stress under both unsaturated and saturated conditions to be converted to effective stress. This conversion provides a superior and convenient approach for evaluating the changes in soil stiffness and strength with the change of the effective stress (or matric suction). The suitability and applicability of the generalized effective stress principle for predicting the unsaturated soil behavior (i.e. shear strength, deformation, and pore pressure generation) has been widely validated by many studies (Ehlers *et al.* 2004; Khalili *et al.* 2004; Chen *et al.* 2009; Borja *et al.* 2012; Oh and Lu 2015;

Downloaded by [International Geosynthetics Society] on [26/03/20]. Copyright © ICE Publishing, all rights reserved.

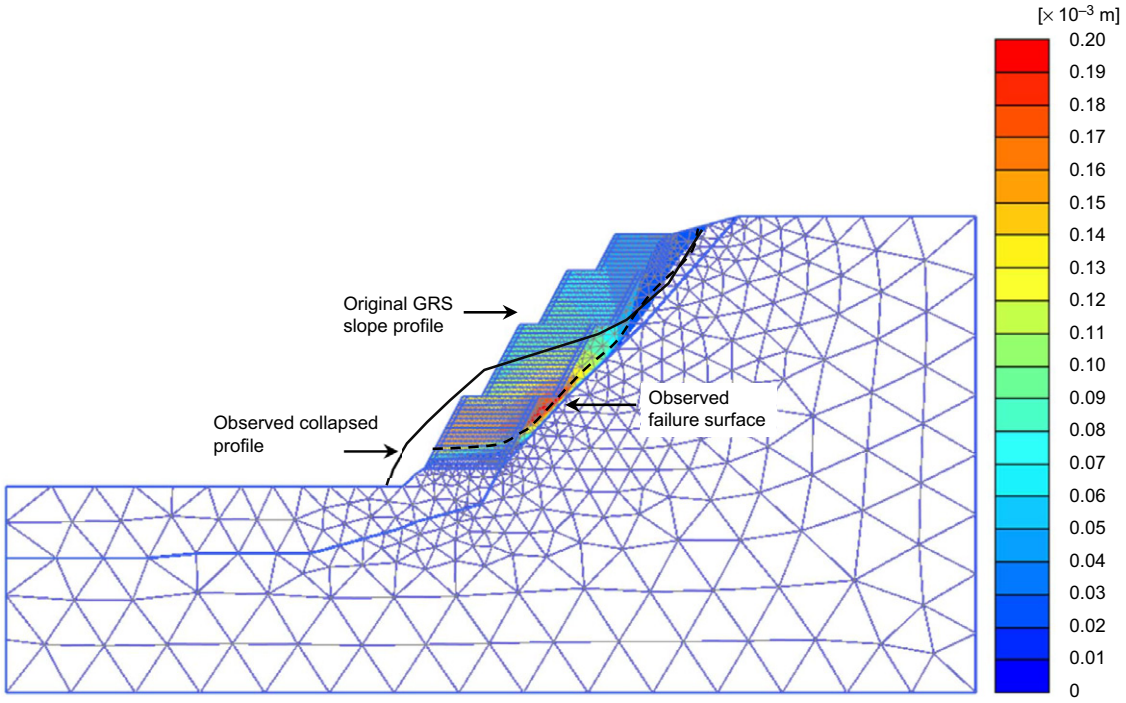

Figure 8. Observed failure surface and FE incremental displacement contours at slope failure

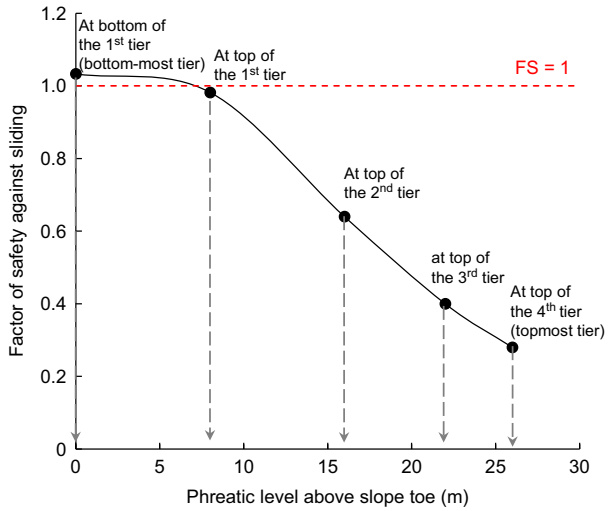

Figure 9. Estimated external stability against sliding at different phreatic levels

Wu *et al*. 2015; Vahedifard *et al*. 2016a). Sheng (2011) concluded that despite challenges associated with obtaining effective stress parameters for soil, the use of Bishop's effective stress for unsaturated soil could enable smooth transitions between saturated and unsaturated states and simplify constitutive relations and shear strength failure criteria.

A general form of the soil effective stress under unsaturated conditions was originally proposed by Bishop (1954, 1959):

$$\sigma' = (\sigma - u_a) + \chi(u_a - u_w) \tag{6}$$

where σ' and σ are the effective and total stress, respectively; $\sigma - u_a$ is the net normal stress; $u_a - u_w$ is the matric suction; χ is the soil parameter in the range of 0 to 1 and is related to the degree of soil saturation, porosity, and matric suction. Bishop (1954) suggested that χ can be substituted by the degree of soil saturation S. In PLAXIS, χ is assumed to be equal to the effective saturation S_e and can be expressed as follows:

$$S_e = \frac{S - S_r}{S_s - S_r} \tag{7}$$

where S is the degree of saturation; S_s is the degree of saturation at the fully saturated state (= 100%); S_r is the degree of saturation at the residual state. The effective stress defined in PLAXIS is identical to that obtained from Equation 8 on the basis of the suction stress concept (Lu and Likos 2004, 2006; Lu *et al*. 2010) because $\Theta = S_e$.

$$\sigma' = (\sigma - u_a) - \sigma^s = (\sigma - u_a) + [\Theta(u_a - u_w)] \tag{8}$$

The suction stress σ^s in Equation 8, can be expressed by forming a suction stress characteristic curve (SSCC), which is a function of matric suction (Lu *et al*. 2010).

$$\sigma^s = -\Theta(u_a - u_w) = -\frac{\theta - \theta_r}{\theta_s - \theta_r}(u_a - u_w) = \frac{-(u_a - u_w)}{\{1 + [\alpha(u_a - u_w)]^n\}^{1-1/n}} \tag{9}$$

where parameters α and n are the curve fitting parameters in the van Genuchten–Mualem model. Suction stress can be perceived as an equivalent isotropic confining stress or mean intergranular stress acting on soil particles, which further increases the soil shear strength. When soil is saturated (i.e. $\Theta = S_e = 1$), the σ^s changes to a positive PWP, and the suction-based effective stress then coincides with Terzaghi's effective stress. The suction stress concept

Downloaded by [International Geosynthetics Society] on [26/03/20]. Copyright © ICE Publishing, all rights reserved.

has been validated experimentally by Kim *et al.* (2016), Oh and Lu (2015), and Morse *et al.* (2014).

Soil shear strength was calculated using the Mohr–Coulomb failure criterion.

$$\tau = c' + \sigma' \tan \phi' \tag{10}$$

where τ is the soil shear strength; c' and ϕ' are the effective cohesion and friction angle, respectively; and σ' is the effective normal stress on the failure plane. When soil is partially saturated, σ' in Equation 8 is substituted into Equation 10:

$$\tau = c' + (\sigma - u_a) \tan \phi' + \Theta(u_a - u_w) \tan \phi' \tag{11}$$

Equation 11 is known as the extended Mohr–Coulomb failure criterion proposed by Vanapalli *et al.* (1996), which can describe and predict the nonlinear relationship between soil strength and suction (Zhang *et al.* 2014; Qi and Vanapalli 2015). When soil is saturated, Equation 11 becomes equivalent to Equation 10, which is valid for the soil shear strength under saturated conditions.

4. NUMERICAL SIMULATION

4.1. Numerical model and boundary conditions

Figure 10 displays the FE model of the GRS slope. The model geometry was constructed according to the topographic map and subsurface soil profile interpolated from the borehole logging readings. Backfill soil (F), weathered sandstone (WR), and fresh shale interbedded with a small amount of sandstone (SH/ss) were considered in the analyses. The numerical model consists of a total of 2685 15-node triangular elements. On the basis of the observed failure mode, because only the backfill soil and weathered rock layer were substantially influenced by rainfall infiltration, a fine-element mesh was specified for the backfill and weathered rock layers whereas a medium-element mesh was applied to the shale layer. The applied mesh densities ensured accurate modeling results and reduced computational cost and time.

Hydraulic and mechanical boundary conditions prescribed in the numerical model are also illustrated in Figure 10. The standard fixity was applied as the mechanical boundary – the two lateral boundaries were allowed to move only in the vertical directions, whereas the bottom boundary was restrained from movement. Examination of the developed stress levels in the numerical models revealed that the assumed mechanical boundary conditions were appropriate.

Hydraulic boundaries at the two lateral ends were initially set to be constant head boundary conditions on the basis of the assumed phreatic level at the toe of the slope (Figure 10). During the analysis, the hydraulic boundaries were switched to the seepage boundary conditions to enable variations in the phreatic level during the wetting and drying cycles. A closed boundary was applied to the base of the slope model to limit the water flowing in and out. Downward vertical influx was prescribed on the slope surface to model rainfall on rainy days, whereas upward influx was imposed on the surface boundary to simulate evapotranspiration on dry days. The input values of downward flux during rainfall were obtained from the actual rainfall records from the nearest rainfall station established by the Taiwan Central Weather Bureau. The value of the upward flux on dry days was estimated to be 6 mm/day in this area, on the basis of the studies on the average evapotranspiration rate of the mountain areas in Taiwan (Chen *et al.* 2005; Hsu *et al.* 2006; Kao *et al.* 2012). Surficial runoff was permitted when the developed PWP on the slope surface changed to a positive value,

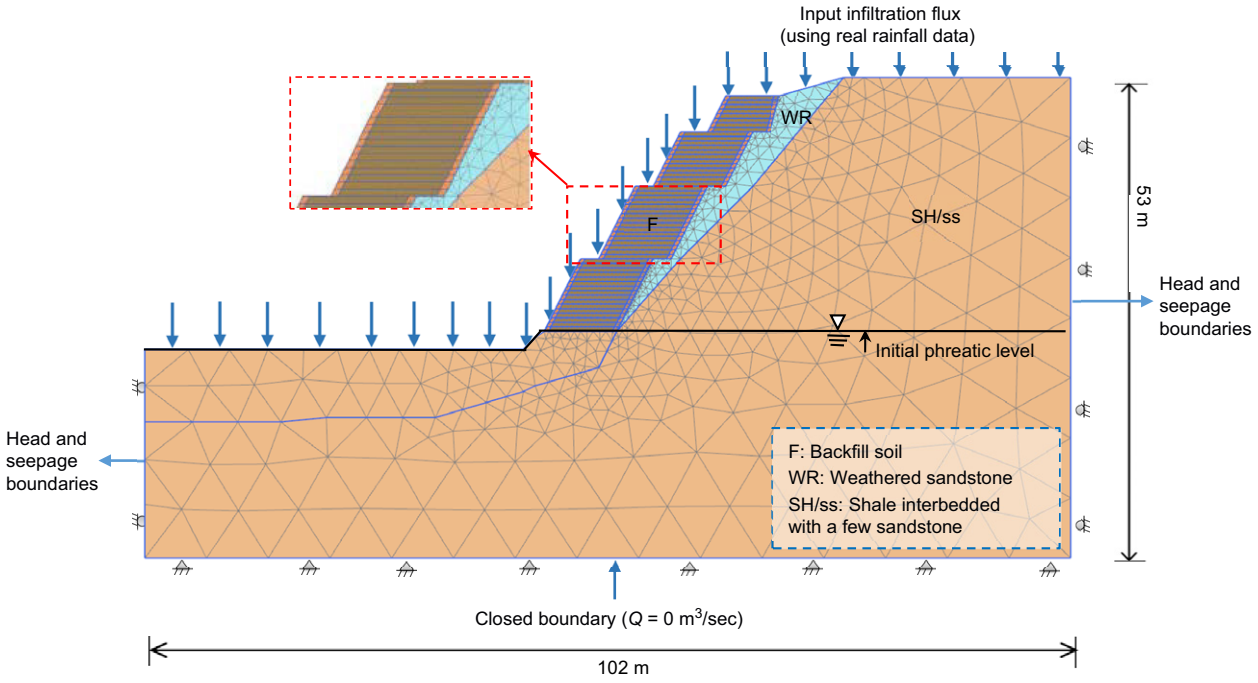

Figure 10. Numerical mesh and boundary conditions

Downloaded by [International Geosynthetics Society] on [26/03/20]. Copyright © ICE Publishing, all rights reserved.

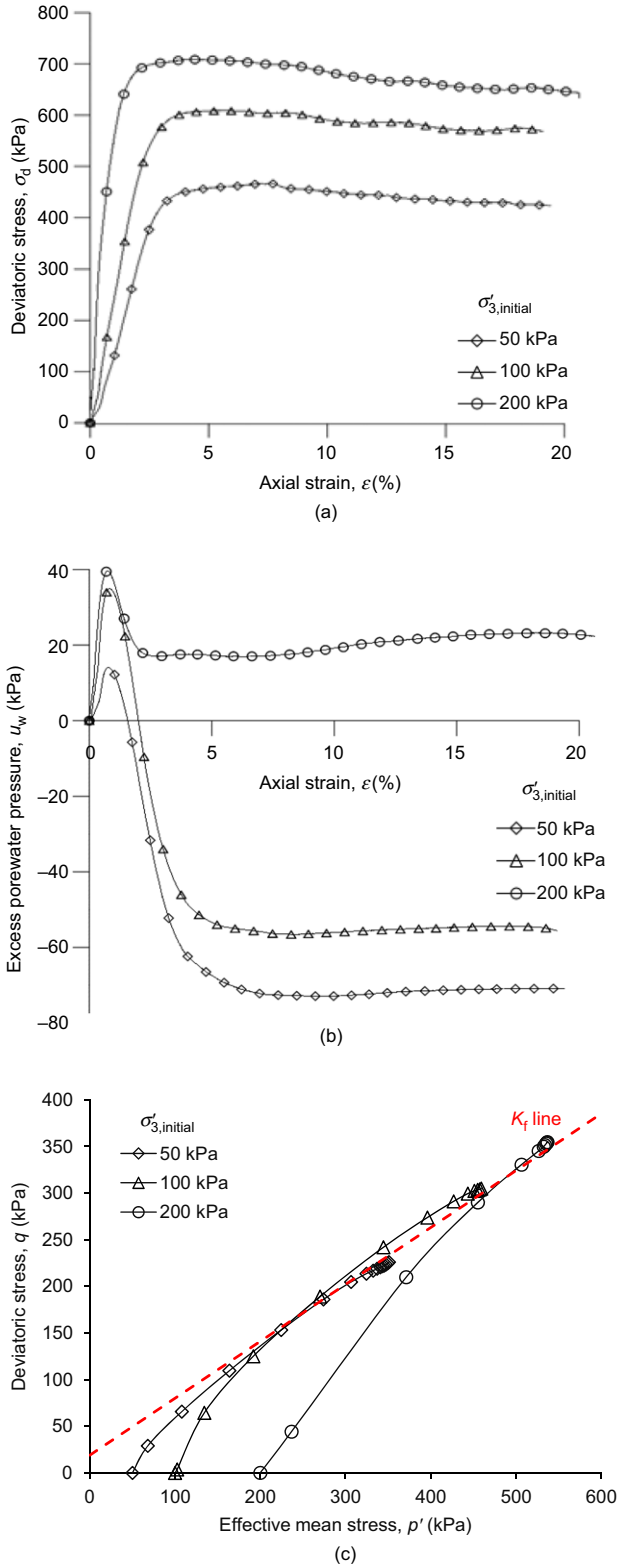

Figure 11. Triaxial CU test results of backfill: (a) stress-strain curve; (b) excess pore water pressure-strain curve; (c) effective stress path

which was achieved by prescribing a maximum PWP value (= 0.01 kPa) on the slope surface. Hence, the water that ponded due to the excess rainfall intensity above the infiltration capacity in the soil saturation state could only accumulate up to 1 mm above the slope surface, and the excess water became runoff.

4.2. Material properties

4.2.1. *Backfill*

The backfill soil specimens were prepared corresponding to the optimum moisture content $\omega_{opt} = 11.8\%$ and maximum dry unit weight $\gamma_{d,max} = 19.3$ kN/m^3 determined from modified Proctor compaction tests. A series of consolidated undrained (CU) triaxial compression tests with pore pressure measurements according to ASTM D4767 was performed to determine the shear strength parameters of the backfill. Figure 11 demonstrates the CU test results and stress paths. On the basis of the test results, the peak shear strength properties of the backfill are the effective friction angle $\phi' = 37°$ and the effective cohesion $c' = 23$ kPa and the residual ones are $\phi' = 37°$ and $c' = 6$ kPa (Table 1). The substantial amount of effective cohesion is possibly due to the compaction-induced soil overconsolidation.

Backfill soil was modeled as a stress-dependent, hyperbolic, elastoplastic material by using the Hardening Soil model (Schanz *et al.* 1999). The nonlinear (hyperbolic) soil stress–strain relation provided in the Hardening Soil model can effectively model the changes of soil modulus at different stress levels, which can appropriately simulate soil deformation at large soil strain conditions. In addition, a stress-dependent soil modulus, implying that the modulus changes as the effective stress changes, is modeled in the Hardening Soil model. The stress-dependent modulus is an essential feature to appropriately describe changes in the soil modulus with matric suction for modeling the unsaturated soil behavior.

The analysis of backfill soil was performed using effective stress parameters under drained conditions. The undrained soil moduli obtained from the CU tests under different confining pressures (Figure 11a) were first converted to the drained soil modulus by using Equation 12, based on the elasticity theory.

$$E'_{50} = E_{50}\frac{2(1+\nu')}{3} \tag{12}$$

where E'_{50} and E_{50} are the drained and undrained soil moduli, respectively, at the 50% stress level and ν' is the effective Poisson's ratio, assumed to be 0.3 for backfill. Thereafter, the value of the reference modulus E_{50}^{ref} in the Hardening Soil model was determined as below:

$$E'_{50} = E_{50}^{ref}\left(\frac{c'\cos\phi' + \sigma'_3\sin\phi'}{c'\cos\phi' + p^{ref}\sin\phi'}\right)^m \tag{13}$$

where p^{ref} is the reference stress (= 1 atm = 101.3 kPa); c' and ϕ' are the effective cohesion and friction angle, respectively; σ'_3 is the effective minor principal stress or effective confining pressure in triaxial tests; and m is the modulus exponent. Soil dilation angle ψ was calculated on the basis of the empirical relationship $\psi = \phi - 30°$ proposed by Bolton (1986). Table 2 lists the input soil parameters of the Hardening Soil model for the backfill.

The backfill saturated hydraulic conductivity was also obtained from triaxial tests on the basis of the permeability test, employing a flexible wall permeameter (ASTM D5084). After the specimens were consolidated in

Downloaded by [International Geosynthetics Society] on [26/03/20]. Copyright © ICE Publishing, all rights reserved.

Table 1. Material properties

Soil/rock layer	Soil model	Analysis type	Dry unit weight, γ_d (kN/m^3)	Saturated unit weight, γ_{sat} (kN/m^3)	Poisson ratio, ν', ν_u	Cohesion, c', $q_u/2$ (kPa)	Friction angle, ϕ', ϕ (°)	Saturated hydraulic conductivity, k_s (m/s)	Young's modulus E, E_u (kPa)
Backfill (F)	Hardening soil	Unsaturated drained	19	21	0.3	23[a], 6[b]	37[a], 37[b]	1×10^{-7}	See Table 2
Weathered sandstone (WR)	Mohr-Coulomb	Unsaturated drained	22	23	0.3	2.7[a], 1.4[b]	33[a], 31[b]	1×10^{-6}	1.16×10^5
Shale interbedded with a little sandstone (SH/ss)	Mohr-Coulomb	Saturated undrained	21	22	0.495	1500	0	1×10^{-10}	1.5×10^6
Sand (S)	Mohr-Coulomb	Saturated/unsaturated[c] drained	16	17	0.3	5	39	1.35×10^{-4}	4.76×10^5

[a]Peak shear strength.
[b]Residual shear strength.
[c]Only used in the remedial measure.

Table 2. Input parameters of backfill for Hardening Soil model

Property	Values
Stiffness properties	
E_{50}^{ref}, secant modulus (kPa)	29 500
E_{oed}^{ref}, tangent oedometer loading modulus (kPa)	20 650[a]
E_{ur}^{ref}, unloading-reloading modulus (kPa)	88 500[b]
ν_{ur}, unloading-reloading Poisson's ratio	0.3
m, modulus exponent	0.5
R_f, failure ratio	0.9
Strength properties	
ϕ', friction angle (degree)	37, 37[c]
c', cohesion (kPa)	23, 6[c]
ψ, dilation angle (degree)	7[d]
Unit weight	
γ_d, dry unit weight (kN/m^3)	19
γ_{sat}, saturated unit weight (kN/m^3)	21

[a]Assumed to be 0.7 E_{50}^{ref} as the default value in PLAXIS.
[b]Assumed to be 3 E_{50}^{ref} as the default value in PLAXIS.
[c]Peak and residual soil shear strength, respectively.
[d]Estimated by $\psi = \phi - 30°$ (Bolton 1986).

the consolidation phase, a back-pressure difference of 20 kPa was introduced to the specimens, and the outflow discharge driven by the pressure difference was measured by a volume gauge. The soil hydraulic conductivity was then calculated using Darcy's law. The average saturated hydraulic conductivity of the backfill determined from the tests was $k_s = 1.85 \times 10^{-8}$ m/s.

In the preliminary analyses, simulations were conducted using the backfill hydraulic conductivity in the range of $k_s = 1.0 \times 10^{-8}$–1.0×10^{-6} m/s. By comparing the predicted slope failure timing with the observed one, a suitable backfill hydraulic conductivity was determined as 1.0×10^{-7} m/s, which is approximately five times higher than the test value. The increase of the k_s value can be justified by the real soil field density being possibly lower than the density of the soil specimens prepared for the permeability tests. This is because the soil density in the field varies between 90–100% of $\gamma_{d,max}$ (i.e. $R_c \geq 90\%$), whereas the soil density for permeability tests was carefully prepared at $\gamma_{d,max}$. In addition, the backfill in the field contains a few stones from the incompletely weathered rock. The presence of these stones could possibly increase the soil permeability in the field; these stones were removed for the permeability test in the laboratory. Many studies have also found that hydraulic conductivity determined in the laboratory could differ with, and typically is higher than, that in the field (Benson *et al.* 1997; Gribb *et al.* 2004; Oh and Lu 2015).

Figure 12 illustrates the hydraulic characteristics of the backfill under unsaturated conditions. The drying soil–water characteristic curve (SWCC) of the backfill was obtained by applying various suction pressures to the soil specimens in the pressure plate test (ASTM D6836). The curve fitting parameters of the drying SWCC of the backfill were determined using the van Genuchten–Mualem model in Equation 4 as follows: $\alpha^d = 0.053$ kPa^{-1}, $n^d = 1.78$, $\theta_s^d = 32.7\%$, and $\theta_r^d = 10\%$. By considering that infiltration is a wetting process, the Kool and Parker (1987) procedure was adopted

Downloaded by [International Geosynthetics Society] on [26/03/20]. Copyright © ICE Publishing, all rights reserved.

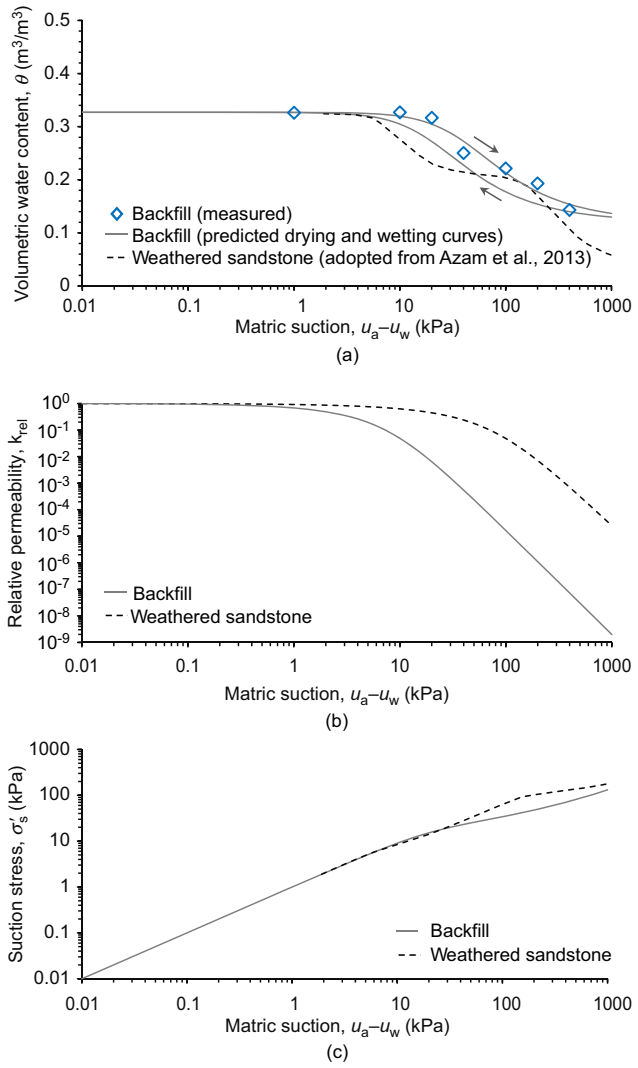

Figure 12. Hydraulic characteristics: (a) soil water characteristic curves (SWCCs); (b) hydraulic conductivity function curves (*k*-function); (c) suction stress characteristic curves (SSCCs)

to approximate the parameters of the wetting curve. In Kool and Parker's procedure, α^d in the drying curve is multiplied by two to obtain α^w in the wetting curve (i.e. $\alpha^w = 2\ \alpha^d$, superscript d and w refers to the main drying and wetting curves, respectively), whereas the other parameters, n, θ_s, and θ_r, remain unchanged. Thus, the fitting parameters for the wetting SWCC of the backfill were estimated as follows: $\alpha^w = 0.106$ kPa^{-1}, $n^w = 1.78$, $\theta_s^w = 32.7\%$, and $\theta_r^w = 10\%$ (Table 3). As shown in Figure 12a, the backfill has an air entry value approximately in the range of 10–20 kPa. Figures 12b and 12c display the hydraulic conductivity function curve (*k*-function curve) and SSCC is calculated using Equations 4 and 8, respectively. Within the range of matric suction in this study (<100 kPa), the soil hydraulic conductivity decreases and suction stress increases as matric suction increases.

With a concern that the clay minerals of the backfill contain montmorillonite, which could cause a significant change in the soil volume upon wetting (Mitchell and Soga 2005), an X-ray diffraction test was conducted to identify and quantify clay minerals in the backfill.

Table 3. Hydraulic characteristic properties

Parameter	Backfill (F)	Weathered sandstone[a] (WR)	Sand[b] (S)
k_s, Saturated hydraulic conductivity (m/s)	1×10^{-7}	1×10^{-6}	1.35×10^{-4}
θ_s, Saturated volumetric water content (%)	32.7	32.4	38
θ_r, Residual volumetric water content (%)	10	21	1
α, van Genuchten model fitting parameter (kPa^{-1})	0.106	0.1	16.67
n, van Genuchten model fitting parameter	1.78	2.8	2.3

[a]For the first part of the SWCC of the weathered sandstone.
[b]Only used in the remedial measure.

The test results revealed that the backfill was composed of illite (83.87%), kaolinite (7.45%), quartz (4.41%), chlorite (2.81%), and feldspar (1.46%). No clay mineral in the smectite group, such as montmorillonite or saponite, was found. As a result, the backfill is not suspected of being expansive and collapsible soil.

4.2.2. *Weathered and intact rock*

Boreholes were drilled from the top of the slope to a depth of 30 m, and the wireline drilling method was employed to obtain rock cores. The weathered sandstone has a low rock quality designation index in the range of RQD = 15–25, which is classified as a fully weathered rock according to Deere and Deere (1988). The peak and residual shear strength properties of the weathered sandstone and the shear strength properties determined from rock direct shear tests are $\phi' = 33°$ and $c' = 2.7$ kPa, and $\phi' = 31°$ and $c' = 1.4$ kPa, respectively (Table 1). The modulus of the weathered sandstone determined from the uniaxial compression test is $E = 1.16 \times 10^5$ kPa. Because only one modulus value was obtained from the test, the Mohr–Coulomb model, a stress-independent model, was selected to model the weathered sandstone, and the analysis was performed using effective stress parameters under drained conditions.

The hydraulic conductivity of the weathered sandstone was estimated to be 1×10^{-6} m/s according to the data of highly disturbed clastic sedimentary rocks in Taiwan reported by Ku *et al.* (2009). The SWCC of the weathered sandstone was adopted from Azam *et al.* (2013). As shown in Figure 12a, the SWCC of the weathered sandstone has a bimodal distribution. The first part of the SWCC has a lower air entry value (<10 kPa), which corresponds to the cracks and fissures of the parent rock, and the second part has a higher value (≈300 kPa) that is associated with the matrix of the decomposed materials. Because the first part of the SWCC covers the range of matric suction in this study (<100 kPa), this part was employed to determine the fitting parameter values (Table 3) and then to develop the *k*-function curve and SSCC of the weathered sandstone (Figures 12b and 12c).

The intact fresh shale layer was modeled using the Mohr–Coulomb model and analyzed by considering

Downloaded by [International Geosynthetics Society] on [26/03/20]. Copyright © ICE Publishing, all rights reserved.

the total stress properties under undrained conditions, because the shale's permeability was relatively low. The hydraulic characteristics of the shale under unsaturated conditions were not considered in the analysis because the rainfall infiltration had a limited impact on the shale layer due to the low permeability of the shale. The shear strength properties and the modulus of the shale were estimated on the basis of the uniaxial compression test results of the shale from the same geological formation reported in literature (Table 1). The saturated hydraulic conductivity of the shale was assumed to be $k_s = 1.0 \times 10^{-10}$ m/s on the basis of the value of a similar type of rock suggested by Goodman (1989).

4.2.3. *Sand*

The sand was used for modeling sandbags at the facings of the slope in the baseline case for failure analysis (Figure 2). Moreover, the sand was employed as a good quality backfill in the parametric study, as discussed later, to assess the effectiveness of remedial measures taken to improve the stability of the GRS slope. The sand was modeled using the Mohr–Coulomb model and analyzed by considering the effective stress parameters under drained conditions. The shear strength and saturated hydraulic conductivity of sand were adopted from the test results reported by Yang *et al.* (2016) (Table 1). By considering that the sand was confined in sandbags, an apparent cohesion of 5 kPa was applied to the sand to account for the confining effect and also to avoid the occurrence of numerical instability (i.e. local soil failure at the slope face) in the numerical simulation.

The hydraulic characteristics of sand under unsaturated conditions were only considered in the remedial measure assessment. The SWCC of sand was estimated using the soil data sets in the USDA soil classification system groups. The predicted SWCC of sand has the following fitting parameters: $\theta_s = 38\%$, $\theta_r = 1\%$, $\alpha = 16.67$ kPa^{-1}, and $n = 2.3$ (Table 3).

4.2.4. *Reinforcement*

The geogrid specimen was retrieved from the failed slope in the field and tested by the single rib tensile method (ASTM D6637) to determine the long-term tensile strength of the geogrid after it was buried for almost 4 years. Figure 13 displays the tensile test results. The tensile strength of the retrieved geogrid is $T_{ult(retrieved)} =$ 113 kN/m, and the secant stiffness at 2% strain is $J_{2\%} = 1250$ kN/m. The long-term strength reduction factor is RF = 1.3 that is calculated by dividing $T_{ult(retrieved)}$ by the ultimate tensile strength of the fresh (new) geogrid specimen $T_{ult(fresh)}$ with a value of 150 kN/m. This RF value is considered very small compared with the total collective reduction value, typically in the range from 5 to 7 as suggested in the design guidelines, accounting for the negative impact from creep, durability, and installation damage. The reinforcement was modeled using a geogrid element with an axial stiffness and tensile strength on the basis of the tensile test results. The soil-reinforcement interface was assumed to be fully bounded in the numerical model, as the primary failure mode of the GRS slope was not governed by the geogrid pullout failure.

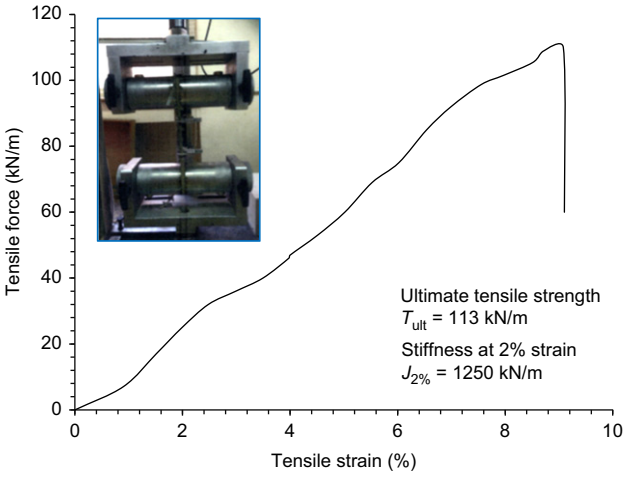

Figure 13. Reinforcement single rib tensile test

4.3. Stage construction and initial conditions

The initial stress condition of the weathered and intact rock layers was first generated using a gravity loading function for non-horizontal strata. Subsequently, the slope construction process involves placing backfill, reinforcements, front and rear sandbags, and wrap-around facings. The placement of these materials was closely simulated in a layer-by-layer stage construction sequence. The 26 m high slope was numerically constructed in 52 steps with an average fill height of approximately 0.5 m, equivalent to the reinforcement vertical spacing.

Upon the completion of the slope construction, the initial PWP was generated by conducting a transient seepage analysis. The influence of modeling antecedent hydrological conditions on the subsequent hydrological modeling has been highlighted in many studies (Blake *et al.* 2003; Yoo and Jung 2006; Oh and Lu 2015; Qi and Vanapalli 2015; Thuo *et al.* 2015). A prescribed flux was specified at the top of the slope model for a considerable duration of time until steady state flow conditions were obtained. The quantities of the prescribed flux were adjusted until the calculated moisture content within the backfill corresponded to the natural gravimetric water content of 13% of the backfill in the field. The matric suction corresponding to this soil moisture condition ranges from 30 to 60 kPa. In addition, the actual rainfall data from 1 July to 20 July 2013, was input as a pre-rainfall event to accurately establish the initial hydrological conditions present immediately prior to the two major typhoon events. Thereafter, the coupled hydro-mechanical analysis was carried out for the two major typhoon events from 20 July to 1 September, 2013.

5. RESULTS AND DISCUSSION

5.1. FS and slope settlement with time

Figure 14a demonstrates the variation in FS and development of slope settlement with rainfall during

Downloaded by [International Geosynthetics Society] on [26/03/20]. Copyright © ICE Publishing, all rights reserved.

two major typhoon events. The observed slope failure timing (1 September 2013) is also indicated in Figure 14. The FS was computed using the *phi/c* reduction function in PLAXIS. In the *phi/c* reduction approach, the shear strength parameters of the soil are successively adjusted until the slope approaches the verge of failure. The numerical results (Figure 14a) indicate that the FS of the slope varied under drying and wetting cycles; the FS of the slope dropped at each rainfall event and recovered during dry days because of the effect of modeling evapotranspiration. The result of the simulation conducted using the residual soil shear strength predicted failure timing at FS = 1, which matched well with that of the observation. The mobilization of the soil residual shear strength within the GRS slope occurred in 2012 when the slope underwent an excessive deformation because the measured maximum slope settlement and facing deflection were 140 and 80 cm, respectively.

Figure 14b displays the predicted slope settlement at the top of each tier. The numerical results reveal that no considerable slope settlement occurred from 20 July to 21 August 2013. A large slope settlement (over 55 mm at the fourth tier) began to develop during Typhoon Trami. Although the development of the settlement ceased after Typhoon Trami, the settlement at each tier again increased substantially during Typhoon Kongrey and reached the maximum value at the observed failure timing.

5.2. Porewater pressure and phreatic level

Figure 15 displays the development of PWP at various locations. The PWP within the backfill (points A and B in Figure 15) increased to 0 kPa (saturated state) after

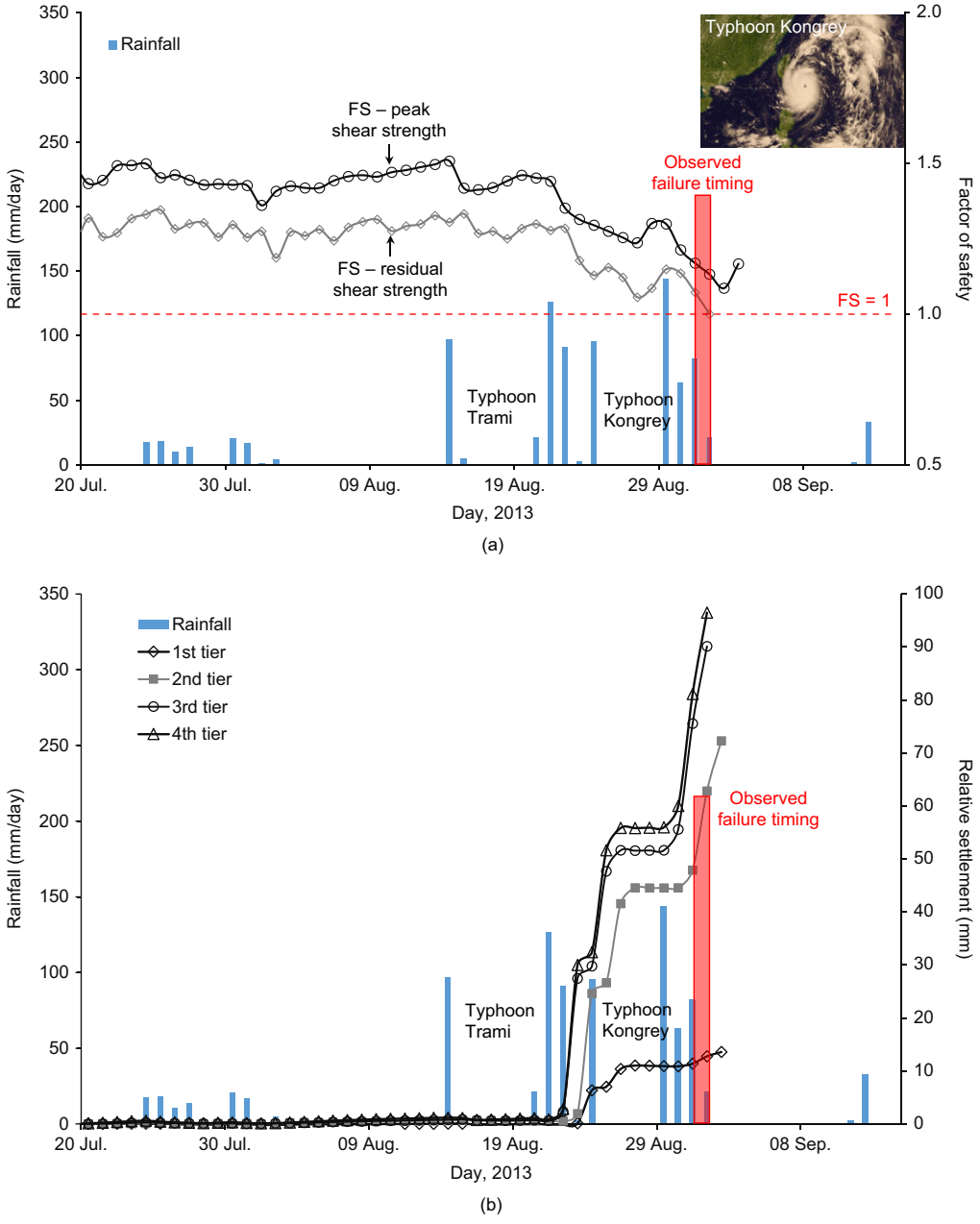

Figure 14. Numerical results: (a) factor of safety; (b) slope settlement

Downloaded by [International Geosynthetics Society] on [26/03/20]. Copyright © ICE Publishing, all rights reserved.

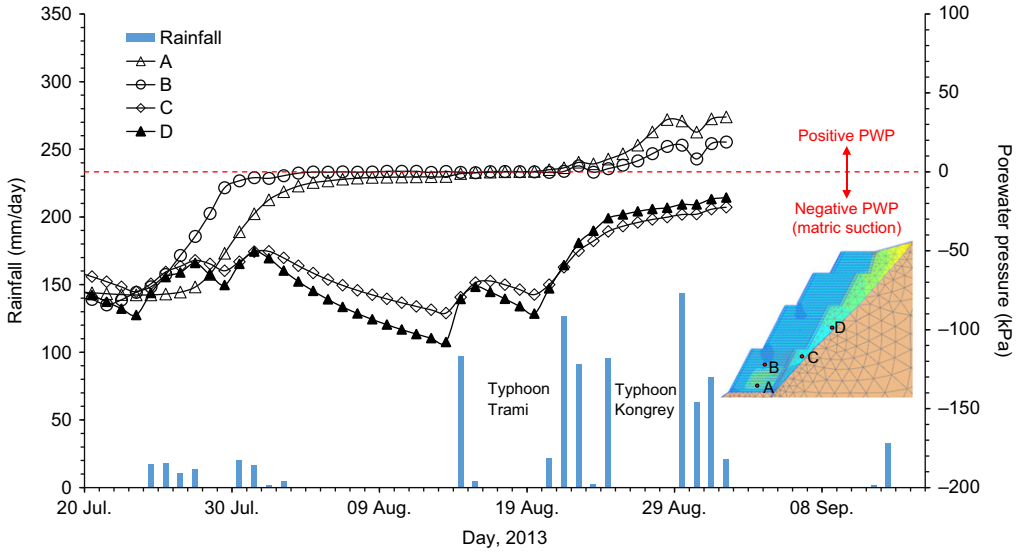

Figure 15. Development of porewater pressure at various locations

the rainfall at the end of July. Owing to the low permeability of the backfill, the PWP could not dissipate effectively, and soil remained fully saturated even during dry days when the evapotranspiration was modeled. The PWP within the weathered sandstone (points C and D in Figure 15) increased during the rainfall at the end of July and then decreased during the dry days. Because the weathered sandstone has a k_s value of one order higher than that of the backfill, the responses of PWPs in the weathered sandstone to weather conditions are much faster than those in the backfill. During the two major typhoon events, the PWPs accumulated and became positive within the backfill, and the PWP within the weathered sandstone gradually increased to a low suction value.

Figure 16 depicts the location of the phreatic surface when the slope failed. At the time of the slope failure, the phreatic level rose to the top of the first tier of the slope. The groundwater fully submerged the bottommost tier and also filled the bottom of the weathered sandstone layer. The phreatic level and PWP distribution predicted from the numerical simulation are supported by the field observation. As shown in Figure 7b, water continued seeping out of the failure part of the backfill. This observation suggested that the soil at the bottommost tier had a high moisture condition, possibly full saturation, and positive PWP possibly accumulated within the backfill. Notably, the location of the predicted phreatic surface in the coupled analysis differs from the one employed in the original design for the slope stability analysis under the heavy rainfall condition (assuming that the phreatic surface is located at the interface between the backfill and the natural slope). The original design misjudged the phreatic level within the slope under the heavy rainfall condition and consequently inaccurately predicted the corresponding value of FS. Finally, the observations of the increased PWP and phreatic level suggest that the infiltrating rainwater could easily accumulate in the marginal backfill. For design implication, efficient and sufficient drainage should be provided, especially at the bottommost tier of the GRS slope where positive PWP could accumulate during rainfall.

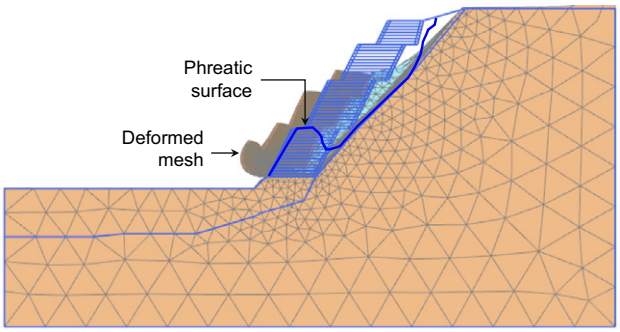

Figure 16. Deformed mesh and phreatic surface at slope failure

5.3. Deformed shape and failure mode

Figure 16 displays the predicted deformed mesh at the slope failure. The GRS slope was pushed by the deformed weathered sandstone, and translational sliding occurred at the bottom of the slope. The deformed shape obtained by prediction is in agreement with that obtained after field observation; that is, the bottom portion of the GRS slope moved out and was suspended from the existing retaining wall (Figure 7b).

Figure 8 illustrates the predicted incremental displacement contours at the slope failure. A locus of the extensive incremental displacement values enables the identification of the location of the potential failure surface. The numerical results suggest that the slope failed in a compound failure mode; this result is in agreement with the observations. The numerical results also reveal that the weathered sandstone became unstable when it was subjected to rainfall infiltration. For design implication, the weathered layer should be stabilized before constructing the GRS structure in front of it.

5.4. Mobilization of reinforcement tensile loads

For the reinforced structure design, the mobilization of reinforcement loads when exposed to rainfall is of

Downloaded by [International Geosynthetics Society] on [26/03/20]. Copyright © ICE Publishing, all rights reserved.

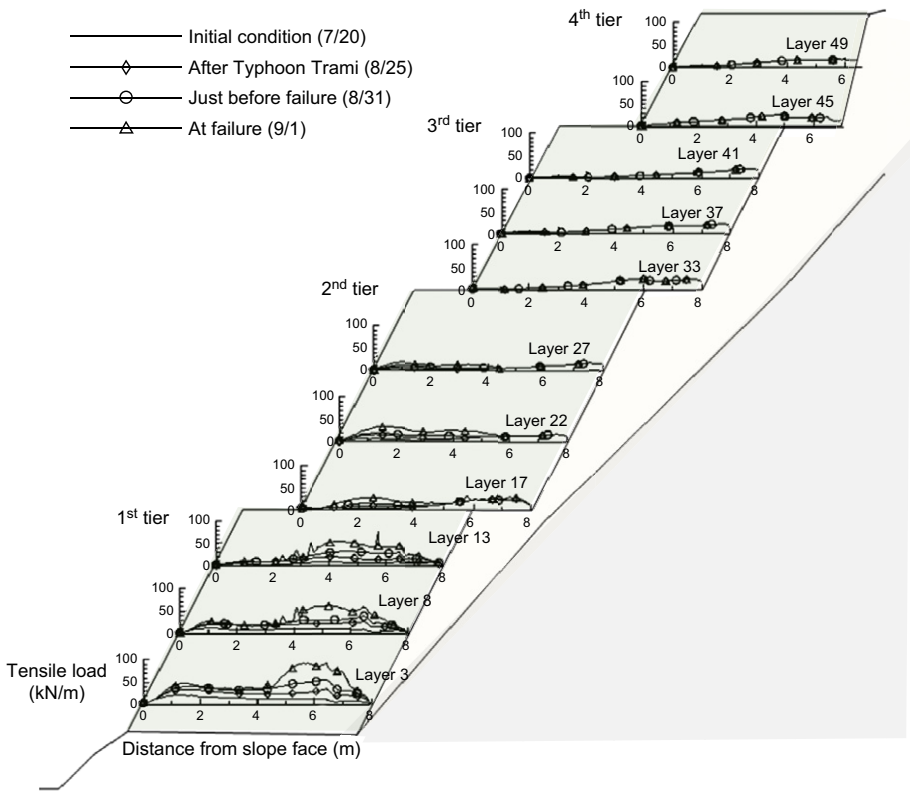

Figure 17. Mobilization and distribution of reinforcement tensile load along reinforcement layer

prime interest. Figure 17 illustrates the mobilization and distribution of reinforcement tensile loads along the reinforcement layer at different timings. Figure 18 displays the profile of the maximum mobilized reinforcement load with the slope height. Because of the modeling of stage construction and initial hydrological conditions, the reinforcement loads at the bottom layer of each tier were mobilized at approximately 20 kN/m in the initial conditions. The mobilized reinforcement loads at the first and second tiers increased as the rainfall progressed. At the slope failure, the reinforcement loads at the first tier were approximately increased to four times those at the initial condition. The increasing reinforcement loads at the two lower tiers (the first and second tiers) were attributed to the decrease in the soil effective stress due to the loss of matric suction and development of positive PWP within the backfill. The reinforcement loads at the upper two tiers (the third and fourth tiers) slightly decreased, thus indicating the release of reinforcement loads possibly due to the soil stress redistribution as the slope deformed. Among all tiers, the reinforcement loads at the first tier were the largest. The mobilized tensile load values in some reinforcement layers were close to the T_{ult} value, as indicated in Figure 18. The substantial mobilization of the reinforcement loads that occurred at the first tier was in accordance with the passage of the failure surface through this tier.

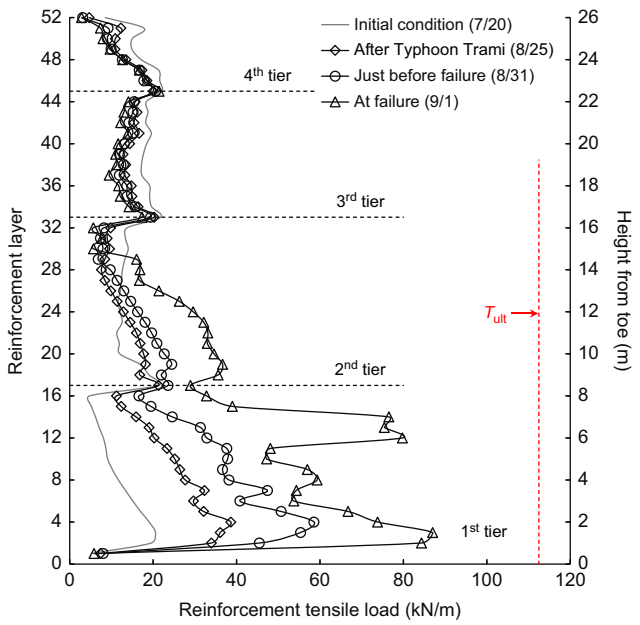

Figure 18. Maximum reinforcement tensile load profile

6. ASSESSMENT OF REMEDIAL MEASURES

On the basis of the failure mechanism interpreted from the failure analysis, a series of parametric studies were conducted to evaluate the remedial measures for improving the system drainage capacity and slope stability of the GRS slope during rainfall. The suggested remedial measures include (1) stabilization of the weathered sandstone layer by using soil nails, (2) provision of a sufficient and efficient drainage system, and (3) use of a good

Downloaded by [International Geosynthetics Society] on [26/03/20]. Copyright © ICE Publishing, all rights reserved.

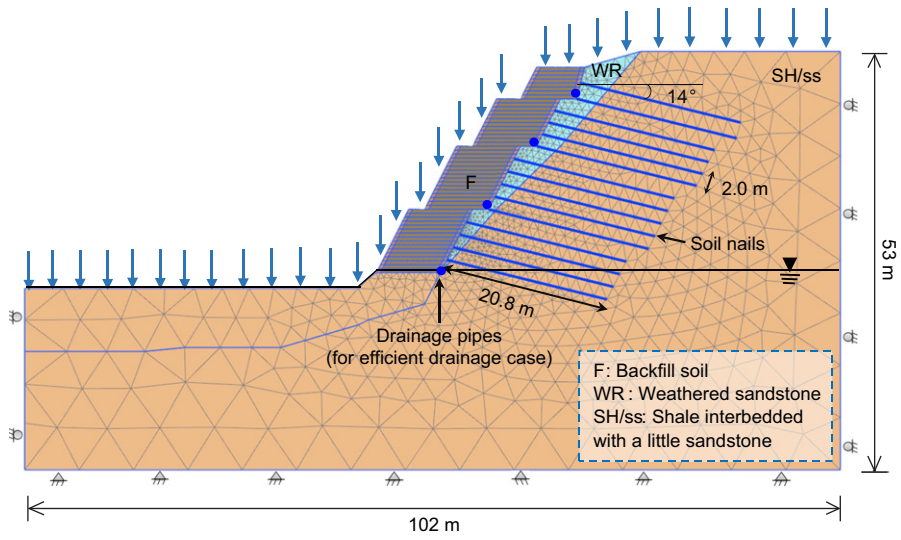

Figure 19. Numerical model for assessment of remedial measures

quality soil as the backfill (e.g. sand backfill). The first remedial measure is known as the shored or hybrid system. Shoring is often employed to stabilize the backslope for a GRS wall constructed in front of it. Morrison *et al.* (2006) highlighted that shoring can reduce lateral loads acting on GRS structures and enhance the global stability of the GRS structure system. Favorable field performance of the shored system has been reported by Fan and Hsieh (2011a 2011b), and Turner and Jensen (2005).

Figure 19 displays the numerical model for the first (using soil nails) and second (using drainage pipes) remedial measures (the two remedial measures are plotted together in Figure 19). In the first remedial measure, soil nails were modeled using embedded beam elements. The nail heads were fixed at the slope face of a weathered sandstone to simulate the fixative effect of the shotcrete facing (Lazarte *et al.* 2015). The soil nails have a diameter of 0.55 m and length of 20.8 m ($=0.8H$, where H is the slope height). The nails are installed in a grid pattern with horizontal and vertical spacings of 1.67 m × 2.0 m and inclination of 14° with respect to the horizontal surface. The adopted inclination angle was within the limits recommended by the design guideline (Lazarte *et al.* 2015) to ensure grout can flow from the bottom of the drill hole to the head. The soil nail has a stiffness of 2.7×10^7 kPa and maximum skin resistance of 430 kN/m, which are calculated from the tributary areas of the active earth pressure diagram. In the second remedial measure, a sufficient and efficient drainage system was modeled by installing drainage pipes at the bottom of each tier. Water was drained freely through the pipe, and no positive PWP was thus allowed to generate at the periphery of the pipe; this was achieved by setting the hydraulic boundary conditions of the pipe as a specified zero pressure-head condition ($h_p = 0$ m) when the positive PWP developed at any node on the pipe surface. In the third remedial measure, sand, a good quality soil, was used as the backfill to replace the marginal soil used in the failure analysis. The properties of sand were discussed previously and are summarized in Table 1. The hydraulic characteristics of sand under unsaturated conditions were considered in the analysis (Table 3).

Figure 20 displays the variation of FSs with time, and Table 4 summarizes the minimum FS values for all remedial measures. The FSs remained greater than 1 (FS > 1.0) for all remedial measures, thus indicating that all the suggested remedial measures can effectively enhance the stability of the GRS slope during rainfall. Compared with the FS value in the baseline case, the second remedial measure (using drainage pipes) demonstrated almost no difference in the FS value before the slope failure. Because the accumulated positive PWP can be dissipated through the drainage pipes, the phreatic level did not rise to the top of the first tier during Typhoon Kongrey (Figure 21). As a result, the FS value remained larger than 1, and the slope maintained its stability at the end of the simulation. In the third remedial measure (using sand backfill), the FS value was low initially because the sand had a low matric suction value at initial conditions. However, the FS value in the good quality backfill case exhibited less variation during rainfall compared with those of other cases. The above observation is supported by Yang *et al.* (2018). Their study found that the stability of the reinforced sand slope was minimally influenced by the loss of matric suction induced by rainfall infiltration. In addition, because of the high-draining capacity of sand, the phreatic level did not increase to the top of the first tier during Typhoon Kongrey (Figure 21). Clearly, the second and third remedial measures can effectively improve the system drainage capacity and thus facilitate PWP dissipation, especially for the PWP developed at the bottom of the slope.

7. CONCLUSIONS

A comprehensive failure investigation of a GRS slope with marginal backfill subjected to rainfall infiltration

Downloaded by [International Geosynthetics Society] on [26/03/20]. Copyright © ICE Publishing, all rights reserved.

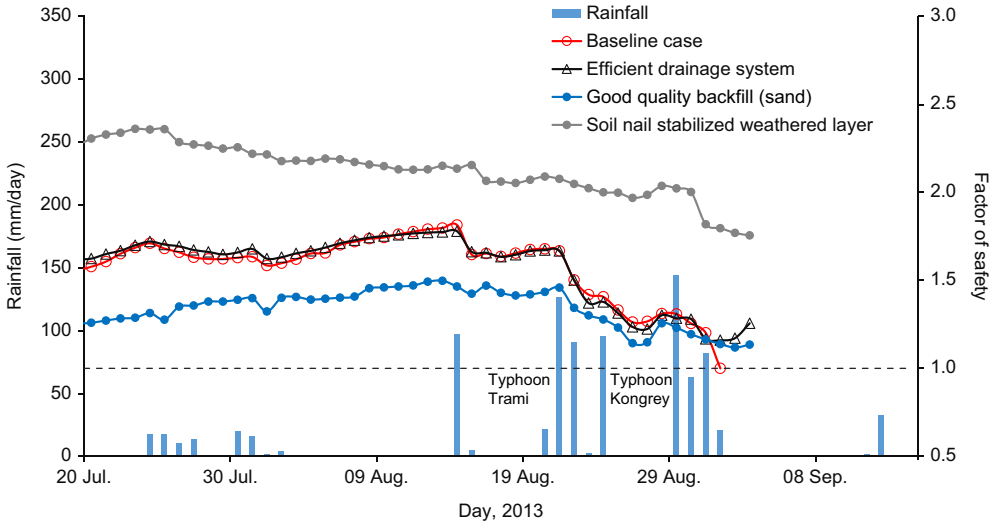

Figure 20. Predicted FS for remedial measure cases

Table 4. Summary of minimum FSs for the suggested remedial measures

Case no.	Description	Minimum FS
Baseline case	Failure analysis	1.00
RM1	Soil nail stabilized weathered layer	1.57
RM2	Efficient drainage system	1.09
RM3	Good quality backfill (sand)	1.07

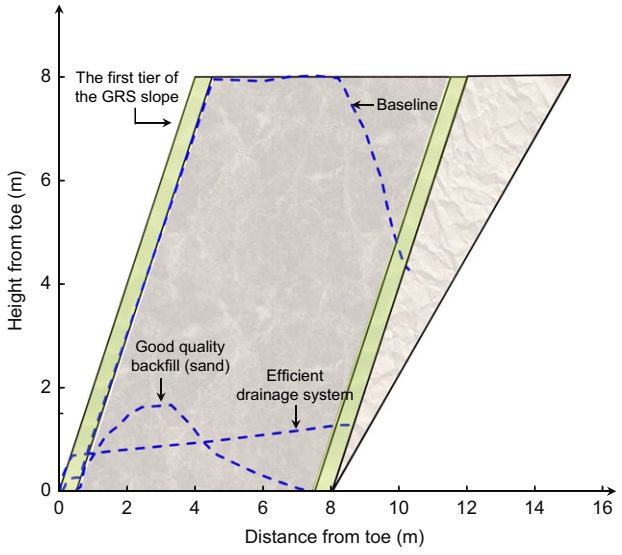

Figure 21. Comparison of phreatic surfaces in the first tier

was conducted in this study. This study demonstrated that by employing recorded rainfall, measured soil parameter, site geology, and slope geometry data in the coupled hydro-mechanical analysis, the failure timing and failure mechanism of a GRS slope can be accurately predicted. The numerical results revealed that the slope failure was due to the increase in PWP (or loss of matric suction). The phreatic level advanced to the weathered rock and increased to the top of the bottommost tier of the GRS slope. The slope failure could be prevented if measures were taken to stabilize the weathered rock layer or provide a sufficient and efficient drainage system.

Three important lessons were learned from this failure investigation. The first lesson learned pertains to the backfill soil and weathered rock. The use of marginal soil as backfill compromises the performance of GRS slopes upon rainfall infiltration. Because of the low draining capacity of the backfill, the PWP could build up inside the slope, and thus cause an excessive slope deformation or even slope failure. In addition, the original site investigation failed to identify the existence of a weak weathered rock layer. An adequately detailed site investigation is required for the design of a GRS structure. Because of the compound failure mode, stabilization of the unstable weathered rock prior to the construction of the GRS slope in front of it is required.

The second lesson learned pertains to the drainage system. Because high positive pore water pressures could accumulate at the slope toe, an appropriate drainage system installation is essential to maintain the slope stability, especially at the bottom tier of the GRS slope. The drainage ditch and impervious layer should be installed at the top of the slope to prevent water infiltration, which could cause subsequently adverse impacts on the slope stability. For a slope backfilled with marginal soil, excessive slope deformation could occur upon rainfall infiltration. Hence, flexible drainage joints should be used to avoid drainage joint disconnection due to slope deformation. The filter criteria should be checked for the nonwoven geotextile or geocomposite used to wrap drainage pipes to avoid long-term clogging of geotextiles by fine soil particles, which can impair or totally disable the system drainage capacity.

The final lesson learned pertains to slope design. In the conventional slope design using the limit equilibrium method, the effect of rainfall on a slope is typically modeled by raising the phreatic level in the slope. However, the original design misjudged the phreatic level within the slope under the heavy rainfall condition

Downloaded by [International Geosynthetics Society] on [26/03/20]. Copyright © ICE Publishing, all rights reserved.

and thus inaccurately predicted the corresponding FS value. For designing GRS structures against rainfall, transient seepage analysis using the regional hydrological data (i.e. the rainfall intensity–duration-frequency IDF curves) should be performed to appropriately understand the soil hydraulic response and predict the location of the phreatic level within the slope. In the transient seepage analysis, the saturated hydraulic conductivity of the soil can be input to produce conservative results if the properties of the unsaturated hydraulic characteristics are not readily available. In addition, the conventional design commonly only considers the internal and global stability of the GRS slope and ignores its external stability. The external stability for the high reinforced slope, which is a function of the geometry and mechanical characteristics of the retained zone and the adjacent topography, could be critical. Therefore, an evaluation of the external stability of the slope should be conducted. As demonstrated in this study, neglecting basic geotechnical engineering principles can result in a major failure.

Finally, the failure case presented in this study should not discourage the application and promotion of GRS structures when granular backfill is not available on site. Instead, the authors intend to highlight that when designing a GRS structure with marginal backfill, special attention should be paid to aspects such as possibly unstable rock slopes, the design and construction of the drainage system, and evaluation of the slope stability, as discussed in this paper.

ACKNOWLEDGEMENTS

The financial support for this research was from the Ministry of Science and Technology of Taiwan under grant no. NSC102-2221-E-011-057-MY3. The third author would also like to acknowledge the financial support for his Ph.D study provided by the Taiwan Ministry of Education under the grant for 'Aim for the Top-Tier University Project'. The authors sincerely appreciate the Taiwan Professional Geotechnical Engineers Association for providing the detailed site investigation information and photographs for the case study in this paper.

NOTATION

Basic SI units are given in parenthesis.

$\boldsymbol{b}$ body force vector (N/m^3)
$\underline{\mathbf{C}}$ coupling matrix (dimensionless)
c' effective cohesion of saturated soil (Pa)
E soil modulus (Pa)
E_u undrained Young's modulus (Pa)
E_{oed}^{ref} tangent oedometer loading modulus (Pa)
E_{ur}^{ref} unloading-reloading modulus (Pa)
E_{50} undrained soil moduli at 50% of stress level (Pa)
E'_{50} drained soil moduli at 50% of stress level (Pa)
E_{50}^{ref} reference modulus (Pa)
FS factor of safety (dimensionless)
$\underline{\boldsymbol{f}_u}$ vector of external load increment (N)
$\underline{\boldsymbol{G}}$ vector of the vertical flow driven by gravity (m/s)
G_s soil specific gravity (dimensionless)
$\boldsymbol{g}$ acceleration of gravity (m/s^2)
$\underline{\boldsymbol{g}}$ vector of gravitational acceleration
H slope height (m)
$\underline{\mathbf{H}}$ permeability matrix (m/s)
h total hydraulic head (m)
h_p pressure head (m)
$J_{2\%}$ secant stiffness at 2% strain (N/m)
$\underline{\mathbf{K}}$ stiffness matrix (N/m)
k hydraulic conductivity (m/s)
k_{rel} relative hydraulic conductivity (dimensionless)
k_s saturated hydraulic conductivity (m/s)
k_x, k_y hydraulic conductivities in the x and y directions (m/s)
L length of the reinforcement (m)
$\underline{\boldsymbol{m}}$ vector with unity for normal stress and zero for shear stress
m modulus exponent (dimensionless)
m_w coefficient of water volume change (Pa^{-1})
n fitting parameter for van Genuchten equations (dimensionless)
n^d fitting parameter for van Genuchten equations for drying curve (dimensionless)
n_p porosity of soil (dimensionless)
n^w fitting parameter for van Genuchten equations for wetting curve (dimensionless)
p pore pressure (Pa)
p' mean effective stress (Pa)
p^{ref} reference stress (Pa)
Q total flux (m^3/s)
$\underline{\mathbf{Q}}$ coupling matrix (dimensionless)
q deviatoric stress (Pa)
$\underline{\boldsymbol{q}_p}$ vector of input flux on boundaries (m/s)
q_u unconfined compression strength (Pa)
R cumulative rainfall (m)
R_c relative compaction (dimensionless)
R_f failure ratio (dimensionless)
RF reduction factor for reinforcement (dimensionless)
S degree of saturation (dimensionless)
$\underline{\mathbf{S}}$ compressibility matrix (Pa^{-1})
S_e effective saturation (dimensionless)
S_r degree of saturation at residual state (dimensionless)
S_s degree of saturation at fully saturated state (dimensionless)
T_{ult} ultimate reinforcement tensile force (N/m)
t time (s)
$\underline{\mathbf{u}}$ vector of incremental deformation (m)
u_a pore air pressure (Pa)
u_w porewater pressure (Pa)
α fitting parameter for van Genuchten equations (Pa^{-1})
α^d fitting parameter for van Genuchten equations on drying curve (Pa^{-1})
α^w fitting parameter for van Genuchten equations on wetting curve (Pa^{-1})
γ unit weight of soil (N/m^3)
γ_d dry unit weight (N/m^3)

Downloaded by [International Geosynthetics Society] on [26/03/20]. Copyright © ICE Publishing, all rights reserved.

$\gamma_{d,max}$ maximum dry unit weight (N/m^3)
γ_{sat} unit weight of saturated soil (N/m^3)
γ_w unit weight of water (N/m^3)
ε axial strain (dimensionless)
Θ normalized volumetric water content (dimensionless)
θ volumetric water content (dimensionless)
θ_r residual volumetric water content (dimensionless)
θ_r^d residual volumetric water content for drying curve (dimensionless)
θ_r^w residual volumetric water content for wetting curve (dimensionless)
θ_s saturated volumetric water content (dimensionless)
θ_s^d saturated volumetric water content for drying curve (dimensionless)
θ_s^w saturated volumetric water content for wetting curve (dimensionless)
ν' drained Poisson's ratio (dimensionless)
ν_u undrained Poisson's ratio (dimensionless)
ν_{ur} unloading-reloading Poisson's ratio (dimensionless)
ρ_w density of water (g/m^3)
σ total stress (Pa)
σ' effective stress (Pa)
σ_d deviatoric stress in triaxial test (Pa)
σ^s suction stress (Pa)
σ'_3 effective minor principal stress (Pa)
$\sigma'_{3,\,initial}$ effective initial confining pressure in triaxial test (Pa)
τ soil shear strength (Pa)
ϕ total friction angle (°)
ϕ' effective friction angle (°)
χ matric suction coefficient (dimensionless)
ψ soil dilation angle (°)
ω_{opt} optimum moisture content (dimensionless)
∇ first order differential operator

REFERENCES

AASHTO (American Association of State Highway and Transportation Officials) (2002). *Standard Specifications for Highway Bridges*, American Association of State Highway and Transportation Officials, Washington, DC, USA.

ASTM D2487 Standard practice for classification of soils for engineering purposes (Unified Soil Classification System). ASTM International, West Conshohocken, PA, USA.

ASTM D4767 Standard test method for consolidated undrained triaxial compression test for cohesive soils. ASTM International, West Conshohocken, PA, USA.

ASTM D5084 Standard test methods for measurement of hydraulic conductivity of saturated porous materials using a flexible wall permeameter. ASTM International, West Conshohocken, PA, USA.

ASTM D6637 Standard test method for determining tensile properties of geogrids by the single or multi-rib tensile method. ASTM International, West Conshohocken, PA, USA.

ASTM D6836 Standard test methods for determination of the soil water characteristic curve for desorption using hanging column, pressure extractor, chilled mirror hygrometer, or centrifuge. ASTM International, West Conshohocken, PA, USA.

Azam, S., Ito, M. & Khan, F. (2013). Influence of cracks on soil water characteristic curve. In *Advances in Unsaturated Soils*, 1st edn, Caicedo, B., Murillo, C., Hoyos, L., Colmenares, J. E. & Berdugo, I. R., Editors, CRC Press, Taylor & Francis Group, London, UK, pp. 217–220.

Balakrishnan, S. & Viswanadham, B. V. S. (2016). Performance evaluation of geogrid reinforced soil walls with marginal backfills through centrifuge model tests. *Geotextiles and Geomembranes*, **44**, No. 1, 95–108.

Benson, C. H., Gunter, J. A., Boutwell, G. P., Trautwein, S. J. & Berzanskis, P. H. (1997). Comparison of four methods to asses hydraulic conductivity. *Journal of Geotechnical and Geoenvironmental Engineering, ASCE*, **123**, No. 10, 929–937.

Berg, R., Christopher, B. R. & Samtani, N. (2009). *Design of Mechanically Stabilized Earth Walls and Reinforced Soil Slopes*, vol. I and II, Report No. FHWA-NHI-10-024. National Highway Institute, Federal Highway Administration, Washington, D.C., USA.

Bhattacherjee, D. & Viswanadham, B. V. S. (2015). Numerical studies on the performance of hybrid-geosynthetic-reinforced soil slopes subjected to rainfall. *Geosynthetics International*, **22**, No. 6, 411–427.

Bishop, A. W. (1954). The use of pore-pressure coefficients in practice. *Geotechnique*, **4**, No. 4, 148–152.

Bishop, A. W. (1959). The principle of effective stress. *Teknisk Ukeblad*, **106**, No. 39, 859–863.

Blake, J. R., Renaud, J. P., Anderson, M. G. & Hencher, S. R. (2003). Prediction of rainfall-induced transient water pressure head behind a retaining wall using a high-resolution finite element model. *Computers and Geotechnics*, **30**, No. 6, 431–442.

Bolton, M. D. (1986). The strength and dilatancy of sands. *Geotechnique*, **36**, No. 1, 65–78.

Borja, R. I., White, J. A., Liu, X. & Wu, W. (2012). Factor of safety in a partially saturated slope inferred from hydro-mechanical continuum modeling. *International Journal for Numerical and Analytical Methods in Geomechanics*, **36**, No. 2, 236–248.

Bui Van, D., Chinkulkijniwat, A., Horpibulsuk, S., Yubonchit, S., Limrat, I., Arulrajah, A. & Jothityangkoon, C. (2017). Steady flow in mechanically stabilised earth walls using marginal soils with geocomposites. *Geosynthetics International*, **24**, No. 6, 590–606.

Chen, J. F., Yeh, H. F., Lee, C. H. & Lo, W. C. (2005). Comparison of empirical equations for estimating potential evapotranspiration in Taiwan. *XXXI IAHR Congress: Water engineering for the future: choices and challenges*, Jun, B.-H., Editor, Korea Water Resources Association, Seoul, Korea, pp. 3687–3697.

Chen, R. H., Chen, H. P., Chen, K. S. & Zhung, H. B. (2009). Simulation of a slope failure induced by rainfall infiltration. *Environmental Geology*, **58**, No. 5, 943–952.

Chinkulkijniwat, A., Horpibulsuk, S., Van, D. B., Udomchai, A., Goodary, R. & Arulrajah, A. (2017). Influential factors affecting drainage design considerations for mechanical stabilised earth walls using geocomposites. *Geosynthetics International*, **24**, No. 3, 224–241.

Christopher, B. R. & Stuglis, R. S. (2005). Low permeable backfill soils in geosynthetics reinforced soil wall: state of the practice in North America. *Proceedings of North American Geo-synthetics Conference (NAGS 2005)*, Las Vegas, NV, USA, GRI-19, pp. 14–16.

Christopher, B. R., Zornberg, J. G. & Mitchell, J. K. (1998). Design guidance for reinforced soil structures with marginal soil backfills. *Proceedings of the 6th International Conference on Geosynthetics: Soil reinforcement applications, geotechnical & hydraulic applications*, Rowe, R. K., Editor, Industrial Fabrics Association International, Atlanta, GA, USA, vol. 2, pp. 797–804.

Deere, D. U. & Deere, D. W. (1988). The rock quality designation (RQD) index in practice. In *Rock Classifications Systems for Engineering Purposes, ASTM STP 984*, Kirkaldie, L., Editor, ASTM International, West Conshohocken, PA, USA, pp. 91–101.

Ehlers, W., Graf, T. & Ammann, M. (2004). Deformation and localization analysis of partially saturated soil. *Computer Methods in Applied Mechanics and Engineering*, **193**, No. 27–29, 2885–2910.

Downloaded by [International Geosynthetics Society] on [26/03/20]. Copyright © ICE Publishing, all rights reserved.

Elias, V., Christopher, B. R. & Berg, R. (2001). *Mechanically Stabilized Earth Walls and Reinforced Soil Slopes Design and Construction Guidelines*, Report No. FHWA-NHI-00-043. National Highway Institute, Federal Highway Administration, Washington, DC, USA.

Fan, C. C. & Hsieh, C. C. (2011a). The mechanical behaviour and design concerns for a hybrid reinforced earth embankment built in limited width adjacent to a slope. *Computers and Geotechnics*, **38**, No. 2, 233–247.

Fan, C. C. & Hsiao, C. F. (2011b). Field performance of a hybrid reinforced earth embankment built adjacent to a slope with narrow fill space. *Journal of GeoEngineering*, **6**, No. 1, 47–62.

Galavi, V. (2016). *Groundwater flow, fully coupled flow deformation and undrained analyses in PLAXIS 2D and 3D*. PLAXIS Internal Research Report, Plaxis BV, Delft, the Netherlands.

Garcia, E. F., Gallage, C. P. K. & Uchimura, T. (2007). Function of permeable geosynthetics in unsaturated embankments subjected to rainfall infiltration. *Geosynthetics International*, **14**, No. 2, 89–99.

Goodman, R. E. (1989). *Introduction to Rock Mechanics*. John Wiley and Sons, New York, NY, USA.

Gribb, M. M., Kodesova, R. & Ordway, S. E. (2004). Comparison of soil hydraulic property measurement methods. *Journal of Geotechnical and Geoenvironmental Engineering, ASCE*, **130**, No. 10, 1084–1095.

Hatami, K. & Esmaili, D. (2015). Unsaturated soil–woven geotextile interface strength properties from small-scale pullout and interface tests. *Geosynthetics International*, **22**, No. 2, 161–172.

Hsu, K. C., Wang, C. H., Chen, K. C., Chen, C. T. & Ma, K. W. (2006). Climate-induced hydrological impacts on the groundwater system of the Pingtung Plain, Taiwan. *Hydrogeology Journal*, **15**, No. 5, 903–913.

Iryo, T. & Rowe, R. K. (2005). Infiltration into an embankment reinforced by nonwoven geotextiles. *Canadian Geotechnical Journal*, **42**, No. 4, 1145–1159.

Kao, Y. H., Liu, C. W., Wang, S. W. & Lee, C. H. (2012). Estimating mountain block recharge to downstream alluvial aquifers from standard methods. *Journal of Hydrology*, **426–427**, 93–102.

Khalili, N., Geiser, F. & Blight, G. (2004). Effective stress in unsaturated soils: review with new evidence. *International Journal of Geomechanics, ASCE*, **4**, No. 2, 115–126.

Kim, W. S. & Borden, R. H. (2013). Numerical simulation of MSE wall behavior induced by surface water infiltration. *Journal of Geotechnical and Geoenvironmental Engineering*, **139**, No. 12, 2110–2124.

Kim, B. D., Park, S. W., Takeshita, Y. & Kato, S. (2016). Effect of suction stress on critical state of compacted silty soils under low confining pressure. *International Journal of Geomechanics, ASCE*, **16**, No. 6, D4016010, https://doi.org/10.1061/(ASCE)GM.1943-5622.0000665.

Koerner, R. M. & Koerner, G. R. (2013). A database, statistics and recommendations regarding 171 failed geosynthetic-reinforced mechanically stabilized earth (MSE) walls. *Geotextiles and Geomembranes*, **40**, 20–27.

Kool, J. B. & Parker, J. C. (1987). Development and evaluation of closed-form expressions for hysteretic soil hydraulic properties. *Water Resources Research*, **23**, No. 1, 105–114.

Ku, C. Y., Hsu, S. M., Chiou, L. B. & Lin, G. F. (2009). An empirical model for estimating hydraulic conductivity of highly disturbed clastic sedimentary rocks in Taiwan. *Engineering Geology*, **109**, No. 3-4, 213–223.

Lazarte, C. A., Robinson, H., Gómez, J. E., Baxter, A., Cadden, A. & Berg, R. (2015). *Geotechnical Engineering Circular No. 7 Soil Nail Walls – Reference Manual*, Publication No. FHWA-NHI-14-007. US Department of Transportation, Federal Highway Administration, Washington, DC, USA.

Liu, C. N., Yang, K. H., Ho, Y. H. & Chang, C. M. (2012). Lessons learned from three failures on a high steep geogrid-reinforced slope. *Geotextiles and Geomembranes*, **34**, 131–143.

Lu, N. & Likos, W. J. (2004). *Unsaturated Soil Mechanics*. John Wiley & Sons, New York, NY, USA.

Lu, N. & Likos, W. J. (2006). Suction stress characteristic curve for unsaturated soil. *Journal of Geotechnical and Geoenvironmental Engineering, ASCE*, **132**, No. 2, 131–142.

Lu, N., Godt, J. W. & Wu, D. T. (2010). A closed-form equation for effective stress in unsaturated soil. *Water Resources Research*, **46**, No. 5, W05515.

Matsumaru, T. & Uzuoka, R. (2016). Three-phase seepage-deformation coupled analysis about unsaturated embankment damaged by earthquake. *International Journal of Geomechanics, ASCE*, **16**, No. 5, C4016006.

Mitchell, J. K. & Soga, K. (2005). *Fundamentals of Soil Behavior*. John Wiley & Sons, New York, NY, USA.

Mitchell, J. K. & Zornberg, J. G. (1995). Reinforced soil structures with poorly draining backfills. Part II: case histories and applications. *Geosynthetics International*, **2**, No. 1, 265–307.

Morrison, K. F., Harrison, F. E., Collin, J. G., Dodds, A. & Arndt, B. (2006). *Shored Mechanically Stabilized Earth (SMSE) Wall Systems Design Guidelines*, Publication No. FHWA-CFL/TD-06-001. US Department of Transportation, Federal Highway Administration, Lakewood, CO, USA.

Morse, M. S., Lu, N., Wayllace, A., Godt, J. W. & Take, W. A. (2014). Experimental test of theory for the stability of partially saturated vertical cut slopes. *Journal of Geotechnical and Geoenvironmental Engineering* **140**, No. 9, 04014050.

Mualem, Y. (1976). A new model for predicting the hydraulic conductivity of unsaturated porous media. *Water Resource Research*, **12**, No. 3, 593–622.

NCMA (National Concrete Masonry Association) (2010). *Design Manual for Segmental Retaining Walls*. NCMA, Herndon, VA, USA.

Oh, S. & Lu, N. (2015). Slope stability analysis under unsaturated conditions: case studies of rainfall-induced failure of cut slopes. *Engineering Geology*, **184**, 96–103.

Portelinha, F. H. M. & Zornberg, J. G. (2014). Development of capillary barriers during water infiltration in a geotextile-reinforced soil wall. *Proceedings of 10th International Conference of Geosynthetics*, Deutsche Gesellschaft Fuer Geotechnik (DGGT), Berlin, Germany, pp. 1–7.

Portelinha, F. H. M. & Zornberg, J. G. (2017). Effect of infiltration on the performance of an unsaturated geotextitle-reinforced soil wall. *Geotextiles and Geomembranes*, **45**, No. 3, 211–226.

Portelinha, F. H. M., Bueno, B. S. & Zornberg, J. G. (2013). Performance of nonwoven geotextile-reinforced walls under wetting conditions: laboratory and field investigations. *Geosynthetics International*, **20**, No. 2, 90–104.

Qi, S. & Vanapalli, S. K. (2015). Hydro-mechanical coupling effect on surficial layer stability of unsaturated expansive soil slopes. *Computers and Geotechnics*, **70**, 68–82.

Raisinghani, D. V. & Viswanadham, B. V. S. (2011). Centrifuge model study on low permeable slope reinforced by hybrid geosynthetics. *Geotextiles and Geomembranes*, **29**, No. 6, 567–580.

Raja, J., Dixon, N., Frost, M. & Zornberg, J. G. (2012). Designing with marginal fills: understanding and practice. *Proceedings of 5th European Geosynthetics Congress*, International Geosynthetics Society, Valencia, Spain, pp. 460–465.

Richards, L. A. (1931). Capillary conduction of liquids through porous mediums. *Physics*, **1**, No. 5, 318–333.

Samtani, N. C. & Nowatzki, E. A. (2006). *Soils and Foundations – Reference Manual*, Publication No. FHWA-NHI-06-088. US Department of Transportation, Federal Highway Administration, Washington, DC, USA.

Schanz, T., Vermeer, P. A. & Bonnier, P. G. (1999). The hardening soil model-formulation and verification. *Beyond 2000 in Computational Geotechnics – 10 Years of Plaxis International; proceedings of the International Symposium Beyond 2000 in Computational Geotechnics*, Brinkgreve, R. B. J., Editor, Balkema, Amsterdam, the Netherlands, pp. 1–16.

Sheng, D. (2011). Review of fundamental principles in modelling unsaturated soil behaviour. *Computers and Geotechnics*, **38**, No. 6, 757–776.

Shibuya, S., Kawaguchi, T. & Chae, J. (2007). Failure of reinforced earth as attacked by typhoon No. 23 in 2004. *Soils and Foundation*, **47**, No. 1, 153–160.

Shou, K. J., Wu, C. C. & Lin, J. F. (2018). Predictive analysis of landslide susceptibility under climate change conditions – a study on the

Downloaded by [International Geosynthetics Society] on [26/03/20]. Copyright © ICE Publishing, all rights reserved.

Ai-Liao watershed in Southern Taiwan. *Journal of GeoEngineering*, **13**, No. 1, 13–27.

Thuo, J. N., Yang, K. H. & Huang, C. C. (2015). Infiltration into unsaturated reinforced slopes with nonwoven geotextile drains sandwiched in sand layers. *Geosynthetics International*, **22**, No. 6, 457–474.

Turner, J. & Jensen, W. G. (2005). Landslide stabilization using soil nail and mechanically stabilized earth walls: case study. *Journal of Geotechnical and Geoenvironmental Engineering*, **131**, No. 2, 141–150.

Vahedifard, F., Leshchinsky, D., Mortezaei, K. & Lu, N. (2015). Active earth pressures for unsaturated retaining structures. *Journal of Geotechnical and Geoenvironmental Engineering, ASCE*, **141**, No. 11, 04015048.

Vahedifard, F., Leshchinsky, D., Mortezaei, K. & Lu, N. (2016a). Effective stress-based limit equilibrium analysis for homogeneous unsaturated slopes. *International Journal of Geomechanics, ASCE*, **16**, No. 6, D4016003.

Vahedifard, F., Mortezaei, K., Leshchinsky, B. A., Leshchinsky, D. & Lu, N. (2016b). Role of suction stress on service state behavior of geosynthetic-reinforced soil structures. *Transportation Geotechnics*, **8**, 45–56.

Vahedifard, F., Tehrani, F. S., Galavi, V., Ragno, E. & AghaKouchak, A. (2017). Resilience of MSE walls with marginal backfill under a changing climate: quantitative assessment for extreme precipitation events. *Journal of Geotechnical and Geoenvironmental Engineering*, **143**, No. 9, 04017056.

Valentine, R. J. (2013). An assessment of the factors that contribute to the poor performance of geosynthetic-reinforced earth retaining walls. *International Symposium on Design and Practice of Geosynthetic-Reinforced Soil Structures*, Ling, H. I., Editor, DEStech Publications, Inc., Lancaster, PA, USA, pp. 318–327.

Vanapalli, S. K., Fredlund, D. G., Pufahl, D. E. & Clifton, A. W. (1996). Model for the prediction of shear strength with respect to soil suction. *Canadian Geotechnical Journal*, **33**, No. 3, 379–392.

van Genuchten, M. T. (1980). A closed form equation for predicting the hydraulic conductivity of unsaturated soils. *Soil Science Society of America Journal*, **44**, No. 5, 892–898.

Viswanadham, B. V. S., Razeghi, H. R., Mamaghanian, J. & Manikumar, C. H. S. G. (2017). Centrifuge model study on geogrid reinforced soil walls with marginal backfills with and without chimney sand drain. *Geotextiles and Geomembranes*, **45**, No. 5 430–446.

Wu, L. Z., Zhang, L. M. & Li, X. (2015). One-dimensional coupled infiltration and deformation in unsaturated soils subjected to varying rainfall. *International Journal of Geomechanics, ASCE*, **16**, No. 2, 06015004.

Yang, K. H., Yalew, W. M. & Nguyen, M. D. (2016). Behavior of geotextile-reinforced clay with a coarse material sandwich technique under unconsolidated-undrained triaxial compression. *International Journal of Geomechanics, ASCE*, **16**, No. 3, 04015083.

Yang, K. H., Thuo, J. N., Huynh, V. D. A., Nguyen, T. S. & Portelinha, F. H. M. (2018). Numerical evaluation of reinforced slopes with various backfill-reinforcement-drainage systems subject to rainfall infiltration. *Computers and Geotechnics* **96**, 25–39, https://doi.org/10.1016/j.compgeo.2017.10.012.

Yoo, C. & Jung, H. Y. (2006). Case history of geosynthetic-reinforced segmental retaining wall failure. *Journal of Geotechnical and Geoenvironmental Engineering, ASCE*, **132**, No. 12, 1538–1548.

Zhang, L. L., Fredlund, D. G., Fredlund, M. D. & Wilson, G. W. (2014). Modeling the unsaturated soil zone in slope stability analysis. *Canadian Geotechnical Journal*, **51**, No. 12, 1384–1398.

Zornberg, J. G. & Mitchell, J. K. (1994). Reinforced soil structures with poorly draining backfills. Part I: reinforcement interactions and functions. *Geosynthetics International*, **1**, No. 2, 103–148.

The Editor welcomes discussion on all papers published in Geosynthetics International. Please email your contribution to discussion@geosynthetics-international.com by 15 August 2019.

Downloaded by [International Geosynthetics Society] on [26/03/20]. Copyright © ICE Publishing, all rights reserved.